Solid Earth

Sedimentary mechanisms of a modern banded iron formation on Milos Island, Greece

Ernest Chi Fru[1,2], **Stephanos Kilias**[3], **Magnus Ivarsson**[4,5], **Jayne E. Rattray**[1], **Katerina Gkika**[3], **Iain McDonald**[2], **Qian He**[6], **and Curt Broman**[1]

[1]Department of Geological Sciences, 10691, Stockholm University, Stockholm, Sweden
[2]School of Earth and Ocean Sciences, Cardiff University, Park Place, CF10 3AT Cardiff, UK
[3]Department of Economic Geology and Geochemistry, Faculty of Geology and Geoenvironment, National and Kapodistrian University of Athens, Panepistimiopolis, Zographou, 15784, Athens, Greece
[4]Department of Biology, University of Southern Denmark, Campusvej 55, Odense M, 5230, Denmark
[5]Department of Palaeobiology, Swedish Museum of Natural History, P.O. Box 50007, Stockholm, Sweden
[6]School of Chemistry, Cardiff University, Park Place, CF10 3AT Cardiff, UK

Correspondence: Ernest Chi Fru (chifrue@cardiff.ac.uk)

Abstract. An early Quaternary shallow submarine hydrothermal iron formation (IF) in the Cape Vani sedimentary basin (CVSB) on Milos Island, Greece, displays banded rhythmicity similar to Precambrian banded iron formation (BIF). Field-wide stratigraphic and biogeochemical reconstructions show two temporal and spatially isolated iron deposits in the CVSB with distinct sedimentological character. Petrographic screening suggests the presence of a photoferrotrophic-like microfossil-rich IF (MFIF), accumulated on a basement consisting of andesites in a ~ 150 m wide basin in the SW margin of the basin. A banded nonfossiliferous IF (NFIF) sits on top of the Mn-rich sandstones at the transition to the renowned Mn-rich formation, capping the NFIF unit. Geochemical data relate the origin of the NFIF to periodic submarine volcanism and water column oxidation of released Fe(II) in conditions predominated by anoxia, similar to the MFIF. Raman spectroscopy pairs hematite-rich grains in the NFIF with relics of a carbonaceous material carrying an average $\delta^{13}C_{org}$ signature of $\sim -25‰$. A similar $\delta^{13}C_{org}$ signature in the MFIF could not be directly coupled to hematite by mineralogy. The NFIF, which postdates large-scale Mn deposition in the CVSB, is composed primarily of amorphous Si (opal-$SiO_2 \cdot nH_2O$) while crystalline quartz (SiO_2) predominates the MFIF. An intricate interaction between tectonic processes, changing redox, biological activity, and abiotic Si precipitation are proposed to have collectively formed the unmetamorphosed BIF-type deposits in a shallow submarine volcanic center. Despite the differences in Precambrian ocean–atmosphere chemistry and the present geologic time, these formation mechanisms coincide with those believed to have formed Algoma-type BIFs proximal to active seafloor volcanic centers.

1 Introduction

Banded iron formations (BIFs) are chemical marine sediments of Precambrian origin (Bekker et al., 2010). They contain at least 15 % bulk Fe content and are characterized by spectacular Fe-rich bands alternating with cherty Si-rich layers (James, 1954; Gross, 1980; Simonson, 1985; Bekker et al., 2010). The interval spanning 3800–1800 million years ago (Ma) records intermittent but widespread BIF deposition on all continents. After a ~ 1000 million year hiatus, BIFs reappeared briefly during the Neoproterozoic Snowball Earth glaciations at ~ 750–550 Ma (Hoffman et al., 1998; Bekker et al., 2010). BIFs are therefore considered a unique feature of a distinct Precambrian ocean–atmosphere chemistry, compared to the fully oxygenated Phanerozoic ocean and atmosphere (Bekker et al., 2010; Poulton and Canfield, 2011).

Recently, a curious ~ 2.0 million year old early Quaternary iron formation (IF) displaying banded rhythmicity typi-
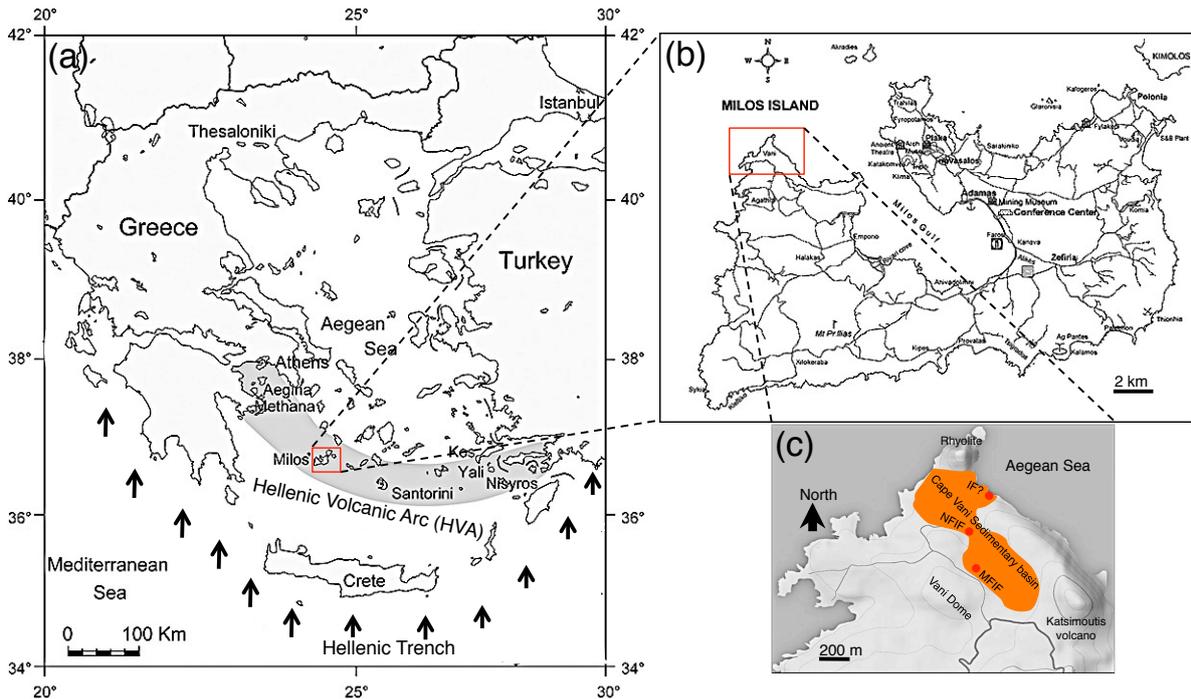
Figure 1. Geological map of Milos (redrawn from Marschik et al., 2010). **(a)** Geotectonic map showing the position of Milos Island, along the Hellenic Volcanic Arc (HVA). Arrows indicate northeast subduction of the African plate underneath the Eurasian plate. **(b)** Milos Island. **(c)** The Milos iron formation is located in the eight-shaped Cape Vani sedimentary basin (CVSB). At least two IFs are present in the CVSB. These are made up of a nonfossiliferous IF (NFIF) at the juncture between the two large sedimentary basins and a microfossiliferous IF (MFIF) located at the SW margin in the second basin. A potential third IF ("IF?" in panel **c**) is located to the NE, close to the present-day Aegean Sea. It is, however, not certain if this deposit is part of the NFIF or not because of the open mining pit separating the two.

cal of BIFs was serendipitously discovered in the Cape Vani sedimentary basin (CVSB), Milos Island, Greece (Chi Fru et al., 2013, 2015). Before this discovery, Cape Vani was long known to host Mn oxide ores of economic potential (Hein et al., 2000; Liakopoulos et al., 2001; Glasby et al., 2005; Kilias et al., 2007). Milos is an emergent volcano on the Hellenic Volcanic Arc (HVA) where arc volcanism and seafloor hydrothermal activity occur in thinned pre-Alpine to Quaternary continental crust (Kilias et al., 2013b) (Fig. 1). The first reported IF from CVSB is unmetamorphosed and contains diverse microfossils encrusted by hematite, with ferrihydrite proposed as a primary precursor mineral (Chi Fru et al., 2013, 2015). Field stratigraphy, rare earth elements (REEs), stable isotopes, and petrographic and microfossil studies point to microbial Fe deposition in a semi-enclosed, shallow submarine basin under conditions analogous to those that formed the Precambrian Algoma-type BIFs near volcanic centers (Chi Fru et al., 2015). These earlier reports assumed a one-time basin-wide depositional event and a common origin for all Fe-rich sedimentary rocks in the CVSB.

However, it remains unclear what sedimentary processes caused the distinct deposition of the BIF-type rocks in a basin where Mn precipitation was apparently widespread at various intervals. Moreover, it is not known how the Mn ores relate

temporally and spatially to Fe deposition in the ~ 1 km long CVSB. This knowledge may provide clues to processes that triggered large-scale deposition of similar Proterozoic Fe–Mn-rich deposits (Roy, 2006; Tsikos et al., 2010; Beukes et al., 2016). Here, new sedimentological, petrological and biogeochemical analyses describe cycles of periodic precipitation of shallow submarine Si- and Fe-rich sedimentary rocks and the plausible mechanisms that enabled their temporal and spatial separation from the Mn deposits in the CVSB. The data reveal a much more complex depositional system not only controlled by microbial Fe(II) oxidation as previously proposed (Chi Fru et al., 2013, 2015) but suggest episodic submarine hydrothermal activity coupled to changing redox conditions as a central mechanism in the formation of the banded iron rocks.

Geological setting

K–Ar radiometric dating of biotite and amphiboles belonging to the dacitic–andesitic lava domes flooring the CVSB gave an upper Pliocene age of 2.38 ± 0.1 Ma (Fytikas et al., 1986; Stewart and McPhie, 2006). Similarly, the presence of the gastropod mollusk, *Haustator biplicatus* (Bronn, 1831), in the fossiliferous sandstones and sandy tuffs hosting the Mn-

rich deposit, indicates a biostratigraphic upper Pliocene to lower Pleistocene age.

The geology and Fe and Mn mineralization of the CVSB have previously been described in detail (Plimer, 2000; Hein et al., 2000; Liakopoulos et al., 2001; Skarpelis and Koutles, 2004; Glasby et al., 2005; Stewart and McPhie, 2006; Kilias, 2011; Alfieris and Voudouris, 2005; Alfieris, 2006; Alfieris et al., 2013; Chi Fru et al., 2013, 2015; Papavassiliou et al., 2017). Briefly, the Milos IF is part of the CVSB, a recently emergent sedimentary rift basin located NW of Milos Island, along the HVA in the Aegean Sea, Greece (Fig. 1). It hosts a fossil analog of active shallow submarine hydrothermal activity on the coast of Milos Island (Dando et al., 1995). The CVSB developed within a shallow submarine rhyolitic-dacitic volcanic center, filled up mainly by a ~ 35–50 m thick stratigraphic succession of volcaniclastic–epiclastic sandstones and sandy tuffs, 35–40 % of which is hydrothermally mineralized by Mn oxides and barite (Hein et al., 2000; Liakopoulos et al., 2001; Skarpelis and Koutles, 2004; Papavassiliou et al., 2017). Sedimentologic and fossil data (trace, bivalves, echinoid, and brachiopod fossils), together with microbially induced sedimentary structures (e.g., Kilias, 2011) suggest that most of the CVSB sandstones and sandy tuffs hosting the Mn-rich deposit, are foreshore to shoreface shallow submarine deposits, formed at a maximum depth of 200 m b.s.l. Over the last 0.8 Myr, fluctuating water depths due to a sea level change of up to 120 m and volcanic edifice building has resulted in tectonic uplift of ~ 250 m (Papanikolaou et al., 1990). The CVSB infill, currently 35 m above sea level, is tectonically bound by extrusive rhyolite to the north, framed by elevated andesitic–dacitic centers, with the Cape Vani and the Katsimoutis dacitic lava domes being the most prominent (Fig. 1).

2 Methodology

2.1 Sample preparation

Prior to mineralogical and geochemical analysis, exposed rock surface layers were sawn and removed. GeoTech Labs (Vancouver, Canada) produced doubly polished thin sections for mineralogical and textural analysis. Trace and rare earth element analysis was performed after digestion of powdered samples with a mixture of acids (HNO_3, HCl, HF) and heat until a clear solution was obtained (Chi Fru et al., 2013, 2015).

2.2 Mineralogical analysis

2.2.1 X-ray diffraction (XRD) analysis

A PANalytical Xpert-pro diffractometer at room temperature, 45 kV, 40 mA, and 1.5406 Å wavelength and Cu-Kα radiation and Ni-filter, was used for powder X-ray diffraction (PXRD) analysis. Samples were analyzed between 5 and 80°

in step sizes of 0.017° with a continuous-mode scanning step time of 50.1650 s while rotating.

2.2.2 Raman spectroscopy

Raman analysis was performed with a confocal laser Raman spectrometer (Horiba instrument LabRAM HR 800), equipped with a multichannel air-cooled (-70 °C) 1024×256 pixel charge-coupled device (CCD) array detector as previously described (Chi Fru et al., 2013, 2015). Spectral resolution was ~ 0.3 cm^{-1} pixel^{-1}. Accuracy was determined by a repeated silicon wafer calibration standard at a characteristic Raman line of 520.7 cm^{-1}.

2.2.3 Transmission electron microscopy

Specimens for transmission electron microscopy (TEM) were prepared from the crushed rock specimen powder. This was followed by dry dispersal onto a 300 mesh holey carbon TEM Cu grid. Microscopy was conducted using a JEOL 2100 TEM with a LaB$_6$ source in the School of Chemistry, Cardiff University, operated at 200 kV. The X-ray energy dispersive spectroscopy (X-EDS) analysis was performed with an Oxford Instrument silicon drift detector (SDD) X-Max^N 80 T.

2.2.4 Scanning electron microscopy

Scanning electron microscopy–energy dispersive spectroscopy (SEM-EDS) analysis was done on a FEI QUANTA FEG 650 ESEM. Images were captured at 5 kV and EDS data collected at 20 kV, using an Oxford T-Max 80 detector (Oxford Instruments, UK). The analyses were performed in low vacuum to minimize surface charging of uncoated samples. EDS elemental maps were collected for 30 min or until the signal had stabilized, indicated by a clear distribution trend. The data were further processed with the Oxford Aztec software.

2.3 Geochemical analysis

2.3.1 Laser ablation–inductively coupled plasma–mass spectrometry and trace element analysis

Laser ablation–inductively coupled plasma–mass spectrometry (LA-ICP-MS) was performed at Cardiff University on polished thin sections. The LA-ICP-MS system comprised a New Wave Research UP213 laser system coupled to a Thermo X Series 2 ICP-MS. The laser was operated using a frequency of 10 Hz at pulse energy of ~ 5 mJ for an 80 µm diameter beam using lines drawn perpendicular to the layering and at a movement speed of 26 µm s^{-1}. Samples were analyzed in time-resolved analysis (TRA) mode using acquisition times of between 110 and 250 s, comprising a 20 s gas blank, 80–220 s ablation, and 10 s washout. Dwell times varied from 2 ms for major elements to 35 ms for low-abundance

trace elements. Blank subtraction was carried out using the Thermo Plasmalab software before time-resolved data were exported to Excel.

Separated and independently pulverized banded layers were digested by lithium borate fusion followed by major, trace and REE analyses using ICP–atomic emission spectrometry–mass spectrometry (ICP-AES-MS) and X-ray florescence (XRF) at Bureau Veritas (Ankara). Geochemical data were compared with previously published results for the more widely investigated Mn deposits (Hein et al., 2000; Liakopoulos et al., 2001; Glasby et al., 2005).

2.3.2 Isotope analysis

C, N, and S isotopic composition for the pulverized samples was determined as previously described (Chi Fru et al., 2013, 2015), following combustion in a Carlo Erba NC2500 analyzer and analyzed in a Finnigan MAT Delta V mass spectrometer, via a split interface to reduce gas volume. Reproducibility was calculated to be better than 0.15‰ for $\delta^{13}C$ and $\delta^{15}N$ and 0.2‰ for $\delta^{34}S$. Total C and N concentrations were determined simultaneously when measuring the isotope ratios. The relative error was $< 1\%$ for both measurements. For carbon isotopic composition of organic carbon, samples were pretreated with concentrated HNO_3 prior to analysis.

2.4 Organic geochemistry analysis

Lipid biomarker and compound-specific $\delta^{13}C$ analyses were executed on powdered samples of sectioned bands from which exposed surface layers had been removed. Modern sediments from Spathi Bay, 36°40′ N, 24°31′ E, southeast of Milos Island, collected by push coring at 12.5 m below the seafloor were freeze-dried prior to extraction to aid the identification of potential syngenetic biomarkers in the Quaternary rocks. Between 4 and 6 g of ground samples were ultrasonically extracted using $3 \times$ methanol, $3 \times (1:1)$ methanol : dichloromethane (DCM), and $3 \times$ DCM, and extracts were combined and dried under N_2. Samples were subsequently redissolved in DCM then methylated following the method of Ichihara and Fukubayashi (2010). The resulting residue was silylated using 20 µL pyridine and 20 µL (N, O-bis-trimethylsilyl)trifluoroacetamide (BSTFA) and heated at 60 °C for 15 min. Total lipid extracts were analyzed using a Shimadzu QP 2010 ultra gas chromatography mass spectrometer (GC/MS). Separation was performed on a Zebron ZB-5HT column (30 m × 0.25 mm × 0.10 µm) with a helium carrier gas flow at 1.5 mL min^{-1}. Samples were injected splitless onto the column at 40 °C with the subsequent oven temperature program ramped to 180 °C at a rate of 15 °C min^{-1}, followed by ramping to 325 °C at a rate of 4 °C min^{-1} and a final hold for 15 min. The MS was set to scan from 50 to 800 m/z with an event time of 0.70 s and a scan speed of 1111 u s^{-1}. All peaks were background subtracted and identification confirmed using the NIST GC/MS

library and literature spectra. Contamination was not introduced into the samples, as blank samples worked up concurrently with the rock fractions had results comparable to the ethyl acetate instrument blank.

2.5 Chemical weathering analysis

A chemical index of alteration (CIA) was used to determine whether variations in chemical weathering intensities, in addition to hydrothermal activity, would deliver materials into the depositional basin from the continent, according to the formula $CIA = Al_2O_3/(Al_2O_3 + CaO + Na_2O + K_2O) \times 100$. Extensively applied, the CIA reveals subtle changes in weathering fluxes (Nesbitt and Young, 1982; Maynard, 1993; Bahlburg and Dobrzinski, 2011), where increasing CIA values generally indicate an amplified chemical dissolution of rocks and a selective release of dissolvable CaO, Na$_2$O, and K$_2$O into solution (Nesbitt and Young, 1982; Maynard, 1993; Bahlburg and Dobrzinski, 2011). The broken rock particles enriched in the poorly soluble Al$_2$O$_3$ fraction, settle to the seafloor as weathered sediments carrying a chemical composition different from the source. In the absence of chemical dissolution, no net chemical change is expected in the composition of sediments compared to the source and thus a low CIA value. CIA values for detritus of 0–55, 55–75, and > 75 are considered unweathered, unweathered to slightly weathered, and weathered to highly weathered, respectively (Nesbit and Young, 1982; Maynard, 1993; Bahlburg and Dobrzinski, 2011).

2.6 Redox analysis

Redox depositional conditions were evaluated using the sequential Fe extraction redox proxy (Poulton and Canfield, 2005, 2011), combined with the REE composition of the sediment (Planavsky et al., 2010).

2.6.1 REE redox analysis

REE data obtained as described in Sect. 2.3.1 were normalized with the North American Shale Composite (NASC) to maintain consistency with previous studies in which NASC-normalized REE data (SN) were reported for the Milos BIF-type rocks (Chi Fru et al., 2013, 2015). The data were further normalized with the Post Archean Australian Shale (PAAS) (McLennan, 1989) standard for comparative purposes, according to Bau and Dulski (1996). Ce anomalies, calculated from Ce / Ce* (Ce$_{(SN)}$/0.5Pr$_{(SN)}$ + 0.5La$_{(SN)}$) and Pr / Pr* (Pr$_{(SN)}$/0.5Ce$_{(SN)}$ + 0.5Nd$_{(SN)}$) values, were considered significant when Ce / Ce* and Pr / Pr* were less than and greater than 1, respectively (Bau and Dulski et al., 1996; Planavsky et al., 2010).
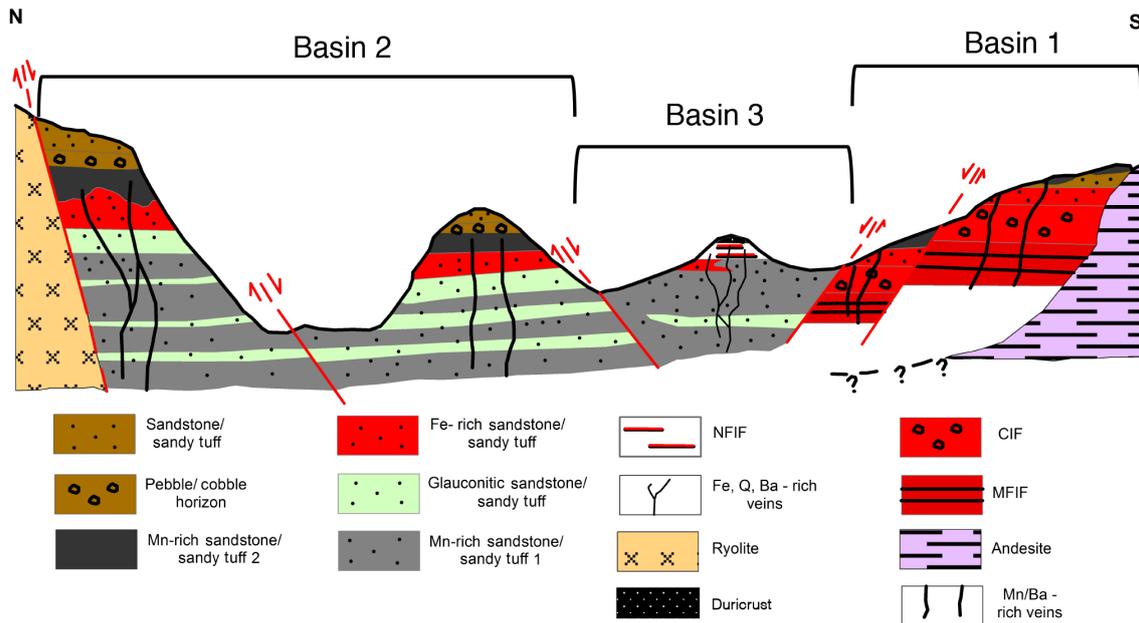
Figure 2. A generalized north–south stratigraphic map of the ∼ 1 km long CVSB showing interpreted geology, lithology, and main faults and how they relate to the iron and manganese formations, in support of a three-basin hypothesis. Not drawn to scale. Four types of iron-rich sedimentary rocks occur in the CVSB. These include the iron-rich sandstones, the iron-Mn-rich sandstones, the CIF, and the MFIF and NFIF formations that are depositionally and chemically distinct from the sandstone deposits.

2.6.2 Sequential iron extraction redox analysis

Analysis was performed on three representative microfossiliferous iron formation (MFIF) samples and the six sectioned bands of a typical nonfossiliferous IF (NFIF) sample using the method developed by Poulton and Canfield (2005) and data interpreted accordingly (e.g., Canfield and Poulton, 2005, 2011; Guilbaud et al., 2015; Sperling et al., 2015). Reagent blanks and geological standards were used for data calibration.

3 Results

Lithostratigraphy

Sedimentary structures, grain size, lateral facies variations, vertical stacking trends, and key stratigraphic surfaces form the basis for facies analysis. Field-wide sedimentological and lithostratigraphical mapping of the CVSB in the summer and fall of 2014 enabled the assessment of the lateral and vertical coverage of the Milos iron-oxide-rich facies relative to the Mn-rich sandstones that dominate the early Quaternary sedimentary basin (Fig. 2). Six stratigraphic sections, representing marine siliciclastic lithofacies sequences, were investigated along a ∼ 1 km SW–NE trending portion of the CVSB infill (Figs. S1–S7 in the Supplement). Sequence stratigraphy was conducted on outcrops and vertical shafts and tunnels left behind by previous Mn mining activity. Two of those sections – Section A located at 36°44′17.85″ N, 24°21′17.72″ E

and Section B located at 36°44′35.11″ N, 24°21′11.25″ E – contain stratigraphic units composed of layered, bedded, or laminated rocks that contain ≥ 15 % Fe, in which the Fe minerals are commonly interlayered with quartz or chert, in agreement with the definition of BIFs (James, 1954; Gross, 1980; Bekker et al., 2010). These IFs are descriptively referred to here as MFIF according to Chi Fru et al. (2013, 2015), and NFIF (this study), respectively (Fig. 2). The MFIF and the NFIF occupy at most ∼ 20 % of the entire CVSB infill. The stratigraphy and sedimentary lithofacies are illustrated in Fig. 2, using lithofacies codes modified after Bouma (1962), Miall (1978, 1985), Mutti (1992), and Shanmugam (2016).

A further field stratigraphic survey revealed considerable lithologic variability within three fault-bounded volcanosedimentary subbasins in the CVSB (Fig. 2), which for the sake of simplicity are referred to as Basin 1 (host of the MFIF), Basin 2 (host of economic-grade Mn ore), and Basin 3 (host of the NFIF) (Fig. 2). Each section is framed by distinct marginal normal faults that strike in the NW–SE and NE–SW to NNE–SSW directions, distinguishable by distinct lateral sedimentary facies exhibiting unique vertical sequence stratigraphy (Figs. 2, S1–S7). Faulting in the CVSB is related to major geographical activation of extensional structures at intervals that shaped Milos into a complex mosaic of neotectonic units (Papanikolaou et al., 1990; van Hinsbergen et al., 2004).
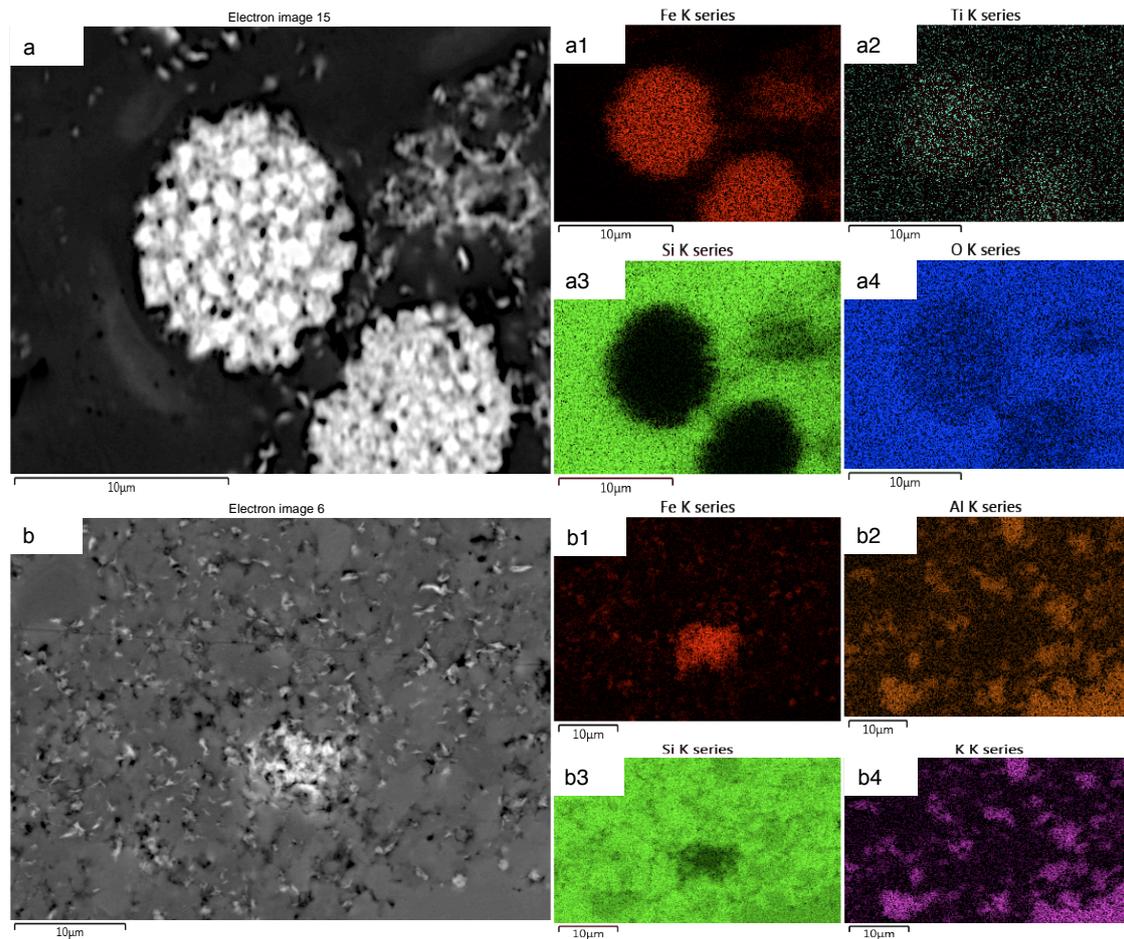
Figure 3. EDS electron micrograph showing Fe-rich mineral phases in a Si-rich matrix from the MFIF. The bright colors correspond to the analyzed elements: **(a)** framboidal hematite particles (**a1–a4**, elemental compositions of the framboidal particles in **a**); **(b)** dispersed fluffy Fe-rich mineral grains (**b1–b4**, corresponding elements associated with the micrograph in panel **a**).

3.1 Section A (36°44′17.85″ N, 24°21′17.72″ E)

Informally known as "Little Vani", Section A is the type section containing the MFIF at the base. It crops out in the W–SW edge of the CVSB (Figs. 1 and 2) as a ~ 6–7 m high cliff resting stratigraphically on submarine dacitic and andesitic lavas and domes. This section extends laterally in the N–NE direction for an estimated 300–500 m.

Lithologically, the MFIF comprises laminated and massive fine-grained red and white weathered ferruginous jaspelitic red chert layers (Chi Fru et al., 2013, 2015). The chert layers contain morphologically distinct Fe minerals dispersed in a fine-grained siliceous matrix (Fig. 3), marked by the notable absence of pyrite and a low S content (Chi Fru et al., 2013, 2015). Layers are tabular and typically laterally continuous at scales of several meters, whereas wave and current structures (e.g., cross-lamination) are generally absent from the MFIF. The hematite-rich MFIF laminae (Table 1) are built by massive encrustation of anoxygenic photoferrotrophic-like microbial biofilms by precipitated Fe (Chi Fru et al., 2013).

The base of the MFIF outcrop is visibly mineralized by black diffused bands or veins composed of Mn oxides (Fig. 4 and Table 1).

A markedly ferruginous 2–3 m thick section immediately overlies the MFIF, comprising a distinct package of Fe-rich beds that transition up the section (Figs. 4a and 5). The lower 1–2 m consist of fine-grained sandstone beds that are well to moderately sorted, containing a 20–40 cm thick portion dominated by plane parallel-laminated sandstone–sandy tuff, massive to plane parallel-laminated sandstone–sandy tuff, and massive sandstone–sandy tuff lithofacies (Figs. 5; S1). The fabric of these Fe-rich sandstone facies consists of sub-angular to subrounded and 100–600 μm fine- to medium-grained volcaniclastic K-feldspar grains, making up up to 75 % of the total rock, with variable amounts of quartz and clay mineral grains.

The latter are overlain by a ~ 1–1.5 m sequence of poorly sorted tabular clast-supported pebble-to-cobble conglomerate beds with an erosional base, grading upward into coarse

Table 1. Results of X-ray diffraction (XRD) analysis showing major mineralogical compositions: NFIF (nonfossiliferous iron formation) and MFIF (microfossiliferous iron formation).

Mineral phase	MFIF1	MFIF2	MFIF3	Fe-rich NFIF2A	Si-rich NFIF2B	Fe-rich NFIF2C	Si-rich NFIFD	Fe-rich NFIF2E	Fe-rich NFIF2F
Hematite	+	+	−	+	+	+	+	+	+
Quartz	+	+	+	−	−	−	−	−	−
Sanidine	−	−	−	+	+	+	+	+	+
Tridymite	−	−	−	−	+	+	+	+	+
Cristobalite	−	−	−	+	−	−	−	−	−
Cryptomelane	−	−	+	−	−	−	−	−	−
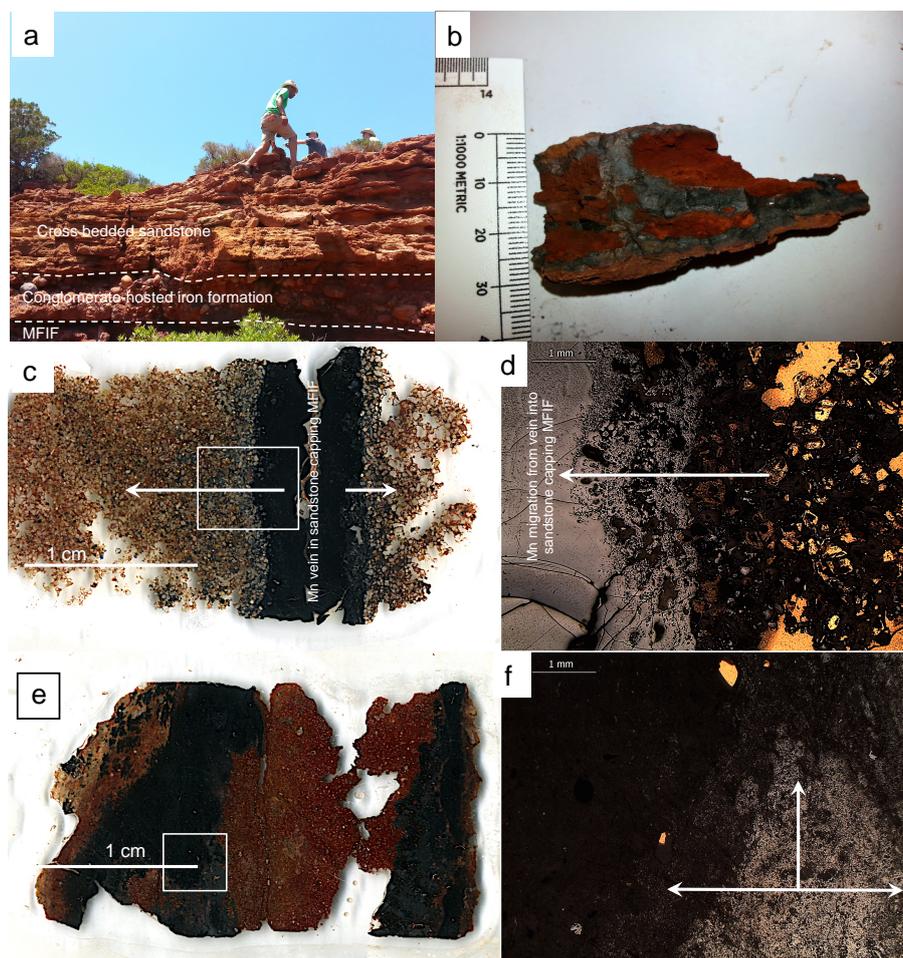
Figure 4. Sedimentary profile, thin section scans and optical microscope images of the MFIF. **(a)** Field photo showing the sedimentary profile of the MFIF characterized by the overlying sandstone cap. **(b)** Photograph showing black diffused Mn-rich bands near the base of the MFIF. **(c)** Scanned image of thin section showing a black Mn-rich vein in the overlying MFIF sandstone showing a gradient of Mn migrating into the sandstone matrix (white arrows). **(d)** Light microscopy images showing details in panel **c**. **(e)** Scanned image of an MFIF thin section showing black Mn band migration into a red iron-rich background. **(f)** Amplified light microscope image showing gray Mn layers migrating into a black Fe-rich matrix. White arrows show direction of movement. Boxes in **(c)** and **(e)** are amplified in **(d)** and **(f)**.

to medium-grained sandstone–sandy tuff beds, with alternating conglomerate cycles (Fig. 5), averaging 20–40 cm in thickness. The cobble–pebble conglomerate clasts include intraformational volcanic rocks (dacite, andesite), al-

lochthonous volcaniclastic sandstone, and volcaniclastic microclasts (e.g., K-feldspar), cemented by hematite (Fig. 5; Chi Fru et al., 2013; Kilias et al., 2013a). Towards the westernmost edge of the Little Vani section, there is a facies
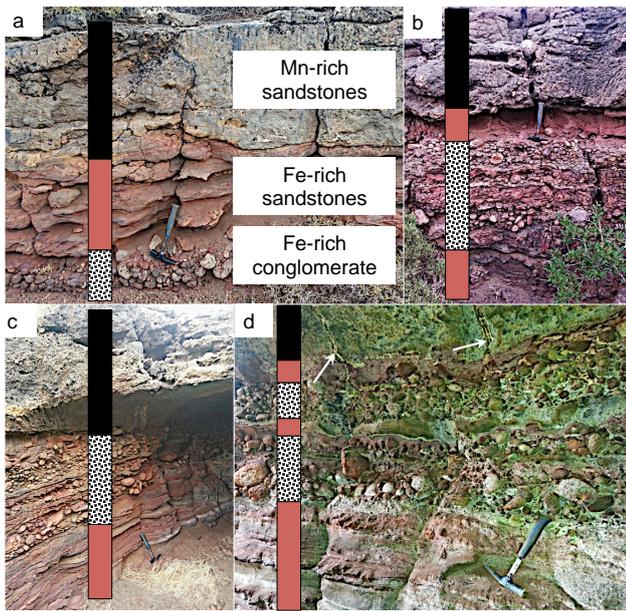
Figure 5. Sedimentary sequence overlying the MFIF, consisting of thin (< 0.5 m) polymictic andesite–dacite cobble–pebble, and sandstone–sandy tuff pebble and Fe-rich conglomerate facies overlain by thinly laminated Fe-rich sandstone beds. This vertical sequence is interpreted as representing a progressively deeper water environment up the sequence (**a**), for reasons including sea level rise due to tectonic subsidence. The multiple cycles in (**b**)–(**d**) suggest potential episodes of sea level change. Arrows in (**d**) show hydrothermal feeder veins feeding the overlying layers. The sequence is overlain by a thin package of parallel and cross-bedded Mn sandstone cap.

Figure 6. Scanning electron microscope micrograph showing the chemical composition of volcaniclast (arrows in **a**) and the iron cement of the CIF overlying the MFIF.

change from the graded pebbly conglomerate and sandy tuff rhythms to a predominantly Fe-rich conglomerate bed (Fig. 6a), termed the conglomerate-hosted IF (CIF) in Chi Fru et al. (2015), with a maximum thickness of ∼ 0.5 m and a cobble size range of ∼ 10 cm. The Fe-rich conglomerate bed transitions upward into medium-grained pebbly reddish ferruginous sandstones with thin volcanic rock and sandstone pebble lenses. This, in turn, grades upwards into a very fine-grained greenish glauconite-bearing plane parallel-laminated sandstone to siltstone bed, characterized by soft-sediment deformation structures, such as flame structures, convolute bedding and lamination structures, loop bedding, load casts, and pseudo-nodules (Figs. 1–2).

The Little Vani section is eventually capped along an erosional surface by an overlying 1–2 m thick section dominated by medium- to fine-grained and moderately to poorly sorted reddish Fe-rich tabular sandstone beds, 10–40 cm thick, topped by patchy sub-centimeter to centimeter-thick Mn-rich sandstones (Figs. 5; S1–S2). Dominant lithofacies of the Fe-rich sandstone cap include planar and hummocky cross-bedding, exhibiting bioturbation in places. The Fe-rich lithofacies cap is laterally discontinuous, thinning out bas-

inwards towards the N–NE and can be observed smoothly grading into a 1–2 m thick section composed of centimeter to sub-centimeter-thick Mn–rich volcaniclastic sandstone lithofacies, described in Sect. 3.2. No Fe-rich hydrothermal feeder veins are obvious in the MFIF. However, feeder veins and Mn horizons can be observed to truncate laminations in the MFIF and up through the whole Little Vani section (e.g., Figs. 4c and 5).

The MFIF rests directly on the submarine dacites–andesites that were deposited in a relatively shallow submarine environment (Stewart and McPhie, 2006). The fine-grained, finely laminated nature of the MFIF and the lack of evidence of current or wave structures (e.g., symmetric ripples or hummocky cross-stratification), coupled to the absence of volcanogenic detrital particles and intraclast breccia structures, indicate a low-energy sedimentation environment, marked by negligible volcanic interference (e.g., Tice and Lowe, 2006; Konhauser et al., 2017). This interpretation is supported by the observed enrichment of Fe in the MFIF, a characteristic of relatively deeper water lithofacies (Konhauser et al., 2017). This view is compatible with the proposition that hematite enrichment in the MFIF was under the control of photoferrotrophic biofilms (Chi Fru et al., 2013) known to thrive at lower light intensities (Kappler et al., 2005; Li et al., 2013; Konhauser et al., 2017). The quiet
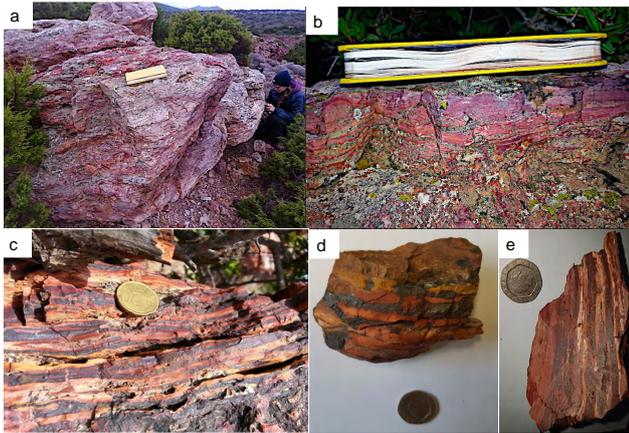
Figure 7. Examples of the NFIF banded iron rocks. **(a–c)** Field photographs. **(d)** Handheld banded Fe sample. **(e)** Sawn NFIF sample with laminated Fe-rich bands alternating with Si-rich bands.

Figure 8. Field sedimentology and stratigraphy of Section B sequence, host to the NFIF. **(a)** Sharp boundary between lower Mn sandstone and unconformably overlying NFIF capped by a ferruginous duricrust. **(b)** Sandstone–sandy tuff pebble to gravel conglomerate facies, showing an upward fining character, locally overlies the Mn sandstone bed and is capped by sharp erosional contact with the overlying NFIF. The tip of the pen (7 cm long) rests on a late blue–black Mn oxide overprint. **(c)** Ferruginous duricrust made up of lithic fragments composed of (1) Fe nodules (2) and Fe concretions (3) in a hematite-rich matrix (4). **(d)** Matrix dissolution resulting in vermiform Mn nodules (1) and cavity black Mn oxide (2) infillings, post-dating the ferruginous duricrust formation.

environmental conditions would have ensured the formation of such stable photoferrotrophic biofilms over extended periods of time that would have facilitated the oxidation of hydrothermally released Fe(II) and the deposition of Fe(III) minerals.

In the overlying sandstone-conglomerate facies, the presence of sedimentary structures indicative of wave action and currents (e.g., cross-stratification), which signify rapid deposition during a high-energy event, are consistent with a switch to a shallow submarine high-energy environment (Stewart and McPhie, 2006; Chi Fru et al., 2015). This shift in depositional environments may have been controlled by a combination of submarine volcano-constructional processes, synvolcanic rifting, and volcano-tectonic uplift known to have formed the CVSB (Papanikolaou et al., 1990; Stewart and McPhie, 2006).

3.2 Section B (36°44′35.11″ N, 24°21′11.25″ E)

This ∼ 8–10 m thick fault-bounded stratigraphic section, here referred to as "Magnus Hill", is the type section that contains the NFIF (Figs. 2, 7 and S3–S4). Two lithostratigraphic units – a lower unit A and an upper unit B – are identified in this study. Unit A is made up of a lower sandstone facies that is ∼ 4–5 m thick, dominated by a Mn oxide cement, overlain by reddish brown Fe-rich massive sandstone beds (Figs. 8 and S3–S4). The lower sandstone facies represents the host of the main economic-grade Mn oxide ores in the CVSB. This constitutes part of a separate study devoted to the Mn ores and will not be dealt with further here. Unit B, ∼ 5 m thick, unconformably overlies unit A and comprises two distinct packages of beds that transition upsection from brownish pebble conglomerate layers (0.5–1.0 m thick) in contact with the very fine-grained NFIF deposit (Figs. S8 and S9). The NFIF is capped by patchy centimeter-thick crustiform Mn oxides. Bifurcating feeder veins composed of

barite, quartz, and Mn–Fe oxide minerals cut through the underlying sandstone beds (Fig. S4).

The NFIF is composed of banded Fe-rich rocks (Fig. 7) exposed on the topmost part of Magnus Hill. About 2–3 m thick, the NFIF consists of millimeter to sub-millimeter thick, dark gray and brown Fe-rich bands, interbanded with reddish brown Si-rich layers (Figs. 7, 9–11, and S10–S11). Sedimentary structures in the NFIF are predominantly characterized by rhythmic millimeter to sub-millimeter thick laminations (e.g., Fig. 7). The iron-oxide-rich bands made up mainly of hematite (Table 1 and Fig. 10c) are typically composed of very fine-grained angular to subangular volcanic dust material (i.e., fine volcanic ash with particle size under 0.063 mm, K-feldspar, tridymite, and cristobalite (Table 1) in an amorphous Si and crystalline hematite matrix (Fig. 12)). The predominantly amorphous Si-rich bands are typically planar, finely laminated, and composed of microcrystalline to cryptocrystalline ferruginous chert.

The NFIF is directly overlain by a ∼ 1 m thick laminated to massive well-indurated, nodular-pisolitic ironstone bed (Fig. 8a, c, and d) that locally preserves a subhorizontal fabric reflecting the bedding in the original sediment or contains various ferruginous clasts such as fragments, nodules, pisoliths, and ooliths set in a hematite-rich siliceous matrix (Fig. 8c). Scattered centimeter-scale pisoliths display a crude concentric internal layering, characterized by open and ver-
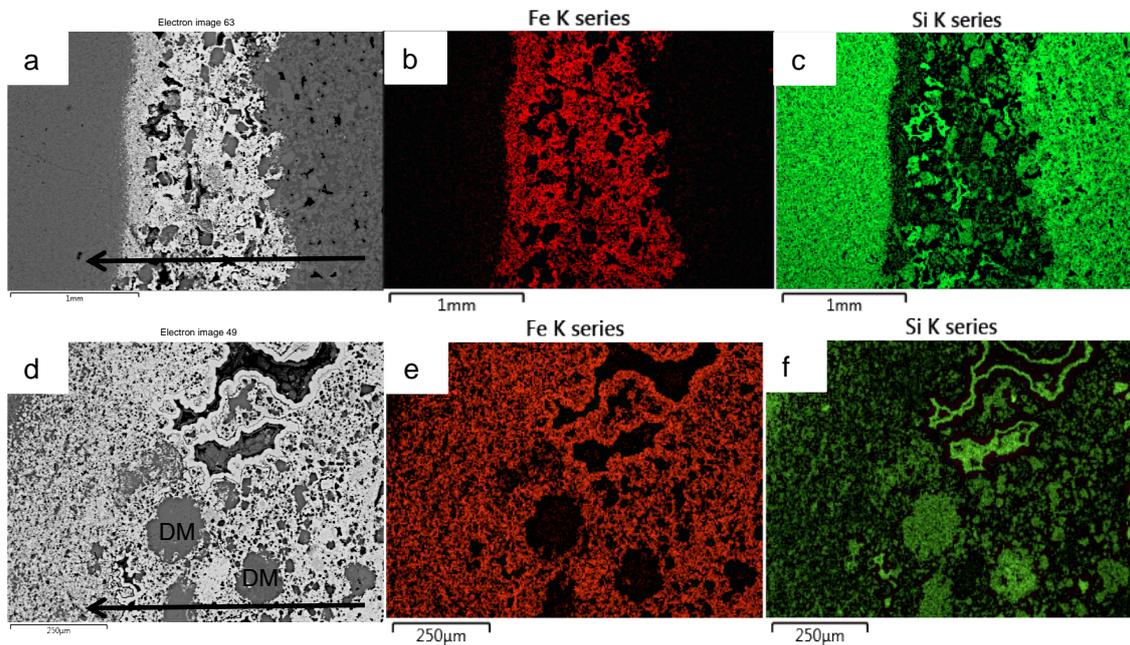
Figure 9. EDS electron micrograph showing major elemental composition of typical Fe bands alternating with Si-rich layers in the NFIF. Volcaniclastic detritus mostly present in the Fe-rich bands suggests precipitation during active submarine volcanism. By contrast, the Si-rich band grains that are of a homogenous fine-size composition and lacking volcaniclast suggest deposition during intervals of minimal volcanic activity. Arrows in **(a)** and **(b)** depict the direction of sedimentation, seen to proceed from an Fe-rich matrix mixed with large grains of volcaniclastic detritus (DM) to one composed essentially of very fine-grained Fe particles before transitioning into the very fine-grained Si-rich layer. An upward fining of the volcaniclastic particles in the Fe-rich layers transitions from one made up of volcaniclastic debris and hematite, to a mainly thin hematite-rich horizon at the top of this mixed layer (see Figs. S8–S11 for details). This concurrent occurrence of volcaniclast and Fe oxides, combined with the upward fining nature of the Fe-rich layers, suggests that the release and oxidation of Fe(II) coincided with the settling of hydrothermal debris resulting from the introduction of an enormous amount of reduced materials into the water column. The Fe-rich layer ceased forming as hydrothermal or volcanic release of Fe subsided, followed by deposition of the Si-rich layer. This repetitive cycle of events is observed for tens of meters laterally and vertically, stressing that the layers are not single isolated or post-depositional replacement events but chemical precipitates that sequentially sedimented out of the water column. Red color in **(b)** and **(c)** depicts Fe, and green in **(c)** and **(f)** depicts Si.

miform voids filled by a cauliflower-like Mn oxide overprint (Fig. 8d). The ferruginous NFIF lithofacies are interpreted as representing the deepest water deposits in the Magnus Hill section based on its very fine-grained sedimentary composition, fine laminations, and a paucity of intraclast breccias. These, combined with the lack of evidence for wave and current-formed sedimentary structures (e.g., hummocky cross-stratification, trough and ripple cross-stratification), indicate quiet-water low-energy sedimentation, likely below the wave base (Simonson and Hassler, 1996; Trendall, 2002; Krapež et al., 2003; Konhauser et al., 2017).

We interpret that each graded Fe-oxide-rich band of the NFIF (Fig. S9), represents an individual fallout deposit from a proximal pyroclastic eruption. This interpretation is supported by gradual grading in fine volcanic ash content of the Fe-rich bands, which suggests that the bands originated from pyroclastic fallout deposits in an otherwise quiet-water setting. For example, tridymite is a stable SiO_2 polymorph formed at low pressures of up to 0.4 GPa and at tempera-

tures of ~ 870–$1470\,°C$ (Swamy et al., 1994; Morris et al., 2016). The coincidence of tridymite formation with silicic volcanism is in agreement with the widespread distribution of andesite, dacite and rhyolite lava domes in the CVSB. For example, vapor phase production of tridymite, together with sanidine mineralization (Fig. 10), are principally associated with rhyolite ash flow (Breitkreuz, 2013; Galan et al., 2013). Similarly, Cristobalite is a SiO_2 polymorph linked with high-temperature rhyolitic eruptions (Horwell et al., 2010). Finally, in situ carbonaceous laminations are absent, suggesting that benthic microbial mat growth had no influence on deposition of the NFIF. Ironstones overlying the NFIF are difficult to interpret with the existing data but may represent supergene ferruginous duricrust formation resulting from subaerial weathering (Anand et al., 2002).
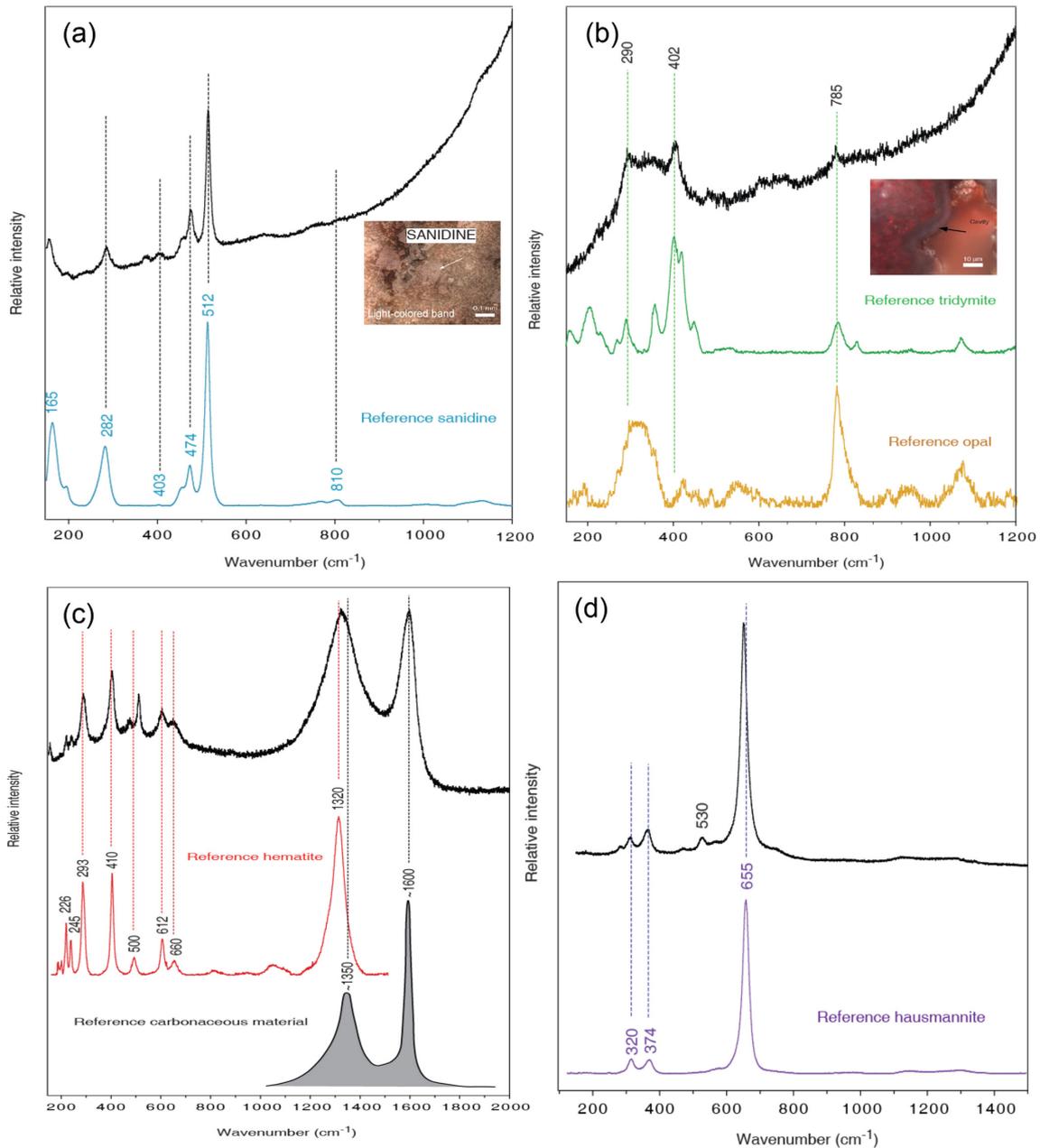
Figure 10. Raman spectroscopy of the Fe-rich and/or Si-rich bands from NFIF.

3.3 Geochemistry

3.3.1 Geochemistry of the individual Fe-rich and Si-rich bands

The SEM-EDS electron micrographs of the NFIF thin sections reveal distinct Fe bands and Si-rich layers alternating periodically with each other in a fine sediment matrix as shown by the grain size (Figs. 9, 11 and S9–S11). Laser ablation ICP-MS line analysis indicates that Si and Fe count intensities in the Milos BIF-type rocks are comparable to the

2.5 Ga Precambrian BIF reference from the Kuruman IF formation, Transvaal Supergroup, South Africa (Fig. 11). The laser ablation ICP-MS data further show an inverse correlation between Fe and Si, the two major elemental components of BIFs, irrespective of the gap of thousands of millions of years separating the Precambrian deposit from the recently formed Milos IF formation.
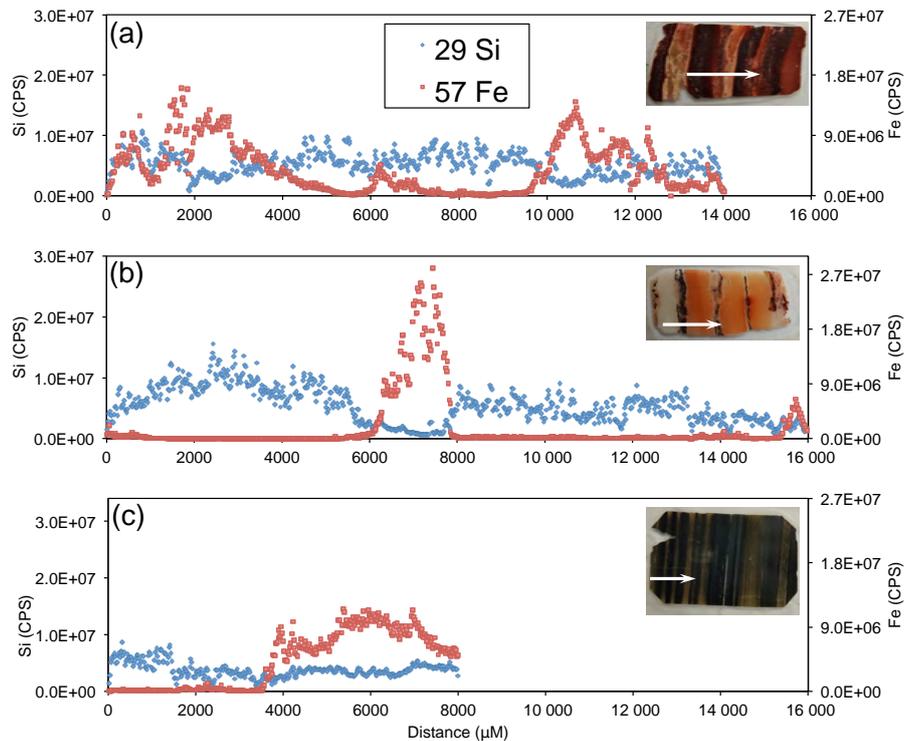
Figure 11. Fluctuation in Si and Fe content measured by in situ laser ablation ICP-MS analysis. **(a)** Milos BIF-type rock with evenly distributed Si- and Fe-rich bands. **(b)** Milos BIF-type rock with wide Si-rich (whitish–brownish strips) and narrow Fe-rich bands (dark strips). **(c)** An example of the 2.5 Ga Kuruman BIF. Insets are analyzed thin sections. For scale, each thin section is ≈ 3.3 cm long, in the direction of the arrows indicating the area analyzed.

3.3.2 Mineralogy of the individual Fe-rich and Si-rich bands

No other Fe(III)(oxyhydr)oxide minerals have been identified in the Cape Vani Fe-rich facies different from hematite. Electron imaging of the NFIF Fe-rich bands suggests Si, Al and K-rich phases are mostly associated with the volcaniclastic material predominated by K-feldspar clasts (Figs. 9, S10 and S11). A unique feature of the NFIF is that the hematite in the Fe-rich bands occurs in tight association with a carbonaceous material (Fig. 10c) but not for the hematite in the Fe-rich sandstones and in the MFIF. This is also the case for the CIF overlying the MFIF. Hematite showing a fluffy texture and at times presenting as framboidal particles is sprinkled in the Si-rich cement containing traces of Al and K in the MFIF rocks (Fig. 3). A lack of association of the framboidal iron-rich particles with S, following SEM-EDS analysis, rules out a pyrite affiliation and is consistent with the non-sulfidic depositional model suggested by the sequential iron extraction redox proxy (Fig. 13d). TEM analysis suggests platy nano-Fe-oxide-rich particles predominate in the NFIF and MFIF, confirmed by overlaid X-ray energy dispersive spectra taken from selected areas (Fig. 12) and consistent with the XRD data showing hematite in both samples. The platy hematite needles in the Milos BIF-type rocks are mor-

phologically, and by size, comparable to hematite needles reported in the ~ 2.5 Ga Kuruman BIFs (Sun et al., 2015).

Unlike the Fe-rich bands, volcaniclasts in the Si-rich bands are much smaller in size, occurring mainly as fine-grained (Figs. S8–S11), signifying predominant precipitation during periods of weakened hydrothermal activity. The SiO_2 matrix in both the MFIF and NFIF is fine-grained, occurring mainly as amorphous opal in the NFIF (Figs. 10b and 12a, b), whereas in the MFIF it is mainly present as crystalline quartz (Fig. 12, d). Relative concentrations of Al, K, and Ti in the samples are generally low, with bulk-measured concentrations in both the Si- and Fe-rich bands, together with the SiO_2 and Fe_2O_3 content, covarying with continental crust concentrations (Fig. 13a). Mn impregnation of the MFIF, preserved in the form of replacement layers mostly identified as cryptomelane ($K(Mn^{4+}, Mn^{2+})_8O_{16}$) (Table 1), is below detection in the NFIF. Rare hausmannite ($Mn^{2+}Mn_2^{3+}O_4$) was detected in a few cases in the MFIF (Fig. 10d).

3.3.3 Hydrothermal versus continental weathering

Trends of major elements from which CIA values were calculated (Fig. 13b), covary with those of the continental crust (Fig. 13a). Continental crust averages, refer to the zone from the upper continental crust to the boundary with the mantle

Table 2. Stable isotope results. Letters A–F on the NFIF samples represent respective bands of the sawn rock in Fig. 7e. PDB: Pee Dee Belemnitel CDT: Canyon Diablo Troilite.

Sample	$\delta^{13}C_{org}$ vs. PDB (‰)	C_{org} (%)	$\delta^{15}N$ vs. air (‰)	N (%)	$\delta^{34}S$ vs. CDT (‰)	S (%)
Fe-rich NFIF2A	−25.63	0.061	nd	0.023	nd	0.01
Si-rich NFIF2B	−25.03	0.109	nd	0.017	nd	0.02
Fe-rich NFIF2C	−24.45	0.068	nd	0.013	nd	0.02
Si-rich NFIF2D	−25.04	0.076	nd	0.015	nd	0.02
Fe-rich NFIF2E	−25.19	0.042	nd	0.009	nd	0.01
Si-rich NFIF2F	−25.49	0.050	nd	0.012	nd	0.03
MFIF1	−25.49	0.087	nd	0.017	nd	0.01
MFIF2	−26.25	0.046	nd	0.005	nd	nd
MFIF3	−25.69	0.041	nd	0,006	nd	nd

Nd: not detected.
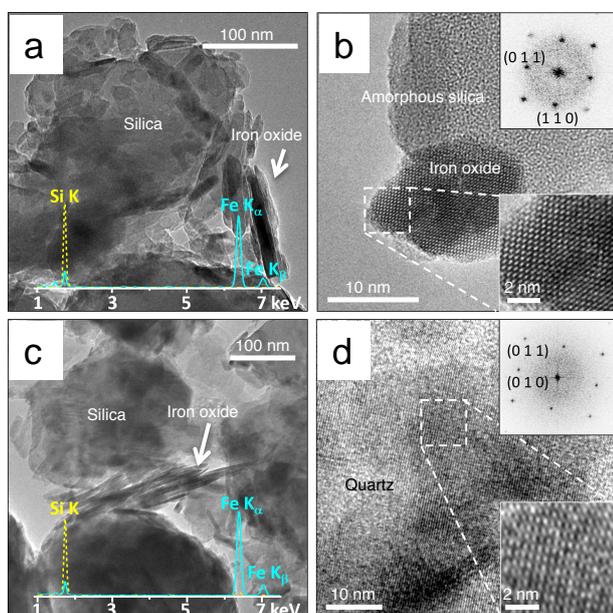
Figure 12. TEM characterization of an NFIF and MFIF specimen. **(a)** Lower-magnification MFIF TEM-BF (bright field) micrograph. **(b)** High-resolution micrograph of NFIF showing amorphous Si and Fe oxide crystalline lattice structures. Insets highlight a hematite particle viewed from the [1–11] axis (rhombohedral lattice). **(c)** Lower-magnification MFIF TEM-BF image. **(d)** High-resolution images of MFIF showing crystalline quartz and iron oxide crystalline lattice structures. Insets in **(d)** show a quartz crystal viewed from the [100] axis. Both samples contain silica with a few hundred nanometer particle size and smaller needle-like iron oxide particles. Spectral lines in panels **(a)** and **(c)** are X-ray energy dispersive elemental profiles of the individual Fe and Si mineral phases.

(Rudnick and Gao, 2003). The calculated CIA values average 52 with one outlier at 22 (Fig. 13b). No distinct relationship could be established between the CIA values and the respective IFs or between the distinct alternating Si- and Fe-rich bands (Fig. 13). Highly weathered clay minerals resulting from the chemical decomposition of volcanic rocks, e.g., kaolinite representing maximum CIA values of 100 or 75–90 for illite, are absent in the analyzed materials. The absence of carbonates in the rocks strengthened the CIA values, since CIA values are expected to be lower when Ca carbonates are present (Bahlburg and Dobrzinski, 2011). TiO_2 content, a detrital proxy, is mostly constant and covaries with the CIA values (Fig. 13b), suggesting little variability and limited continental weathering input. A fairly strong negative linear correlation was found between SiO_2 and Fe_2O_3 values normalized to TiO_2 (inset, Fig. 13b).

3.3.4 Redox reconstruction

Redox reconstruction by sequential iron extraction (Poulton and Canfield, 2005, 2011; Guilbaud et al., 2015; Sperling et al., 2015) is consistent with the deposition of both the MFIF and NFIF facies beneath an anoxic, ferruginous bottom water body (Fig. 13c, d). The shale-normalized REE values ($REE_{(SN)}$) for both the MFIF and NFIF are consistent with previous reports (Chi Fru et al., 2013, 2015), showing patterns typical of marine sedimentary environments affected by hydrothermal activity throughout Earth's history (e.g., Planavsky et al., 2010). There is a notable absence of significant negative $Ce_{(SN)}$ anomalies for both the MFIF and NFIF (Fig. 14a, b). These observations are statistically corroborated by true Ce anomalies. Further, the Eu / Eu* anomaly averages for the MFIF and NFIF and the distinct Fe- or Si-rich bands, suggest a $\sim 2 \times$ higher Eu / Eu* signal for the Si-rich bands relative to the Fe-rich bands and between the MFIF and NFIF deposits (Fig. 14c). Average Pr and Yb shale-normalized ratios (Pr / Yb*), a light vs. heavy REE enrichment proxy (Planavsky et al., 2010), indicate similar depleted levels of light and heavy REE in both the NFIF and MFIF, as well as in the Fe- and Si-rich bands (Fig. 14c). This independent verification of the anoxic depositional conditions using the sequential Fe proxy, suggests that the NASC
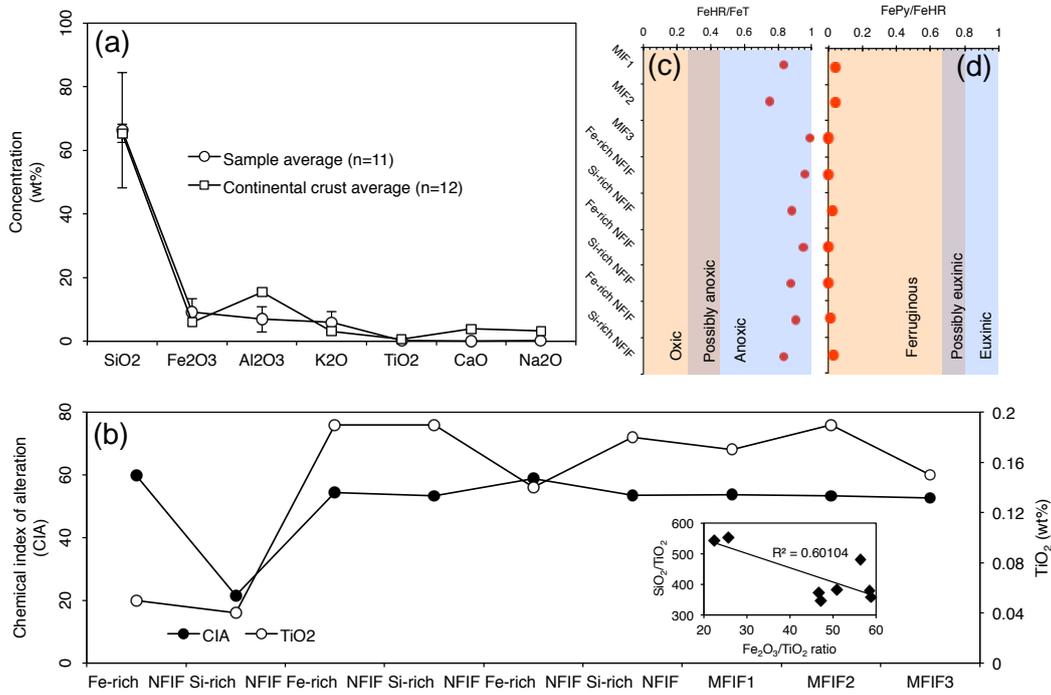
Figure 13. Bulk average concentrations of major trace elements, chemical weathering indices, and reconstructed redox depositional conditions for typical MFIF and the Fe- or Si-rich NFIF bands for the sawn rock sample in Fig. 7e. **(a)** Relationship between average major trace element content and average continental crust (Rudnick and Gao, 2003). **(b)** CIA. Inset, relationship between SiO_2 and Fe_2O_3. **(c)** Highly reactive Fe (FeHR) to total Fe ratio (FeT). **(d)** Pyrite to FeHR ratio.
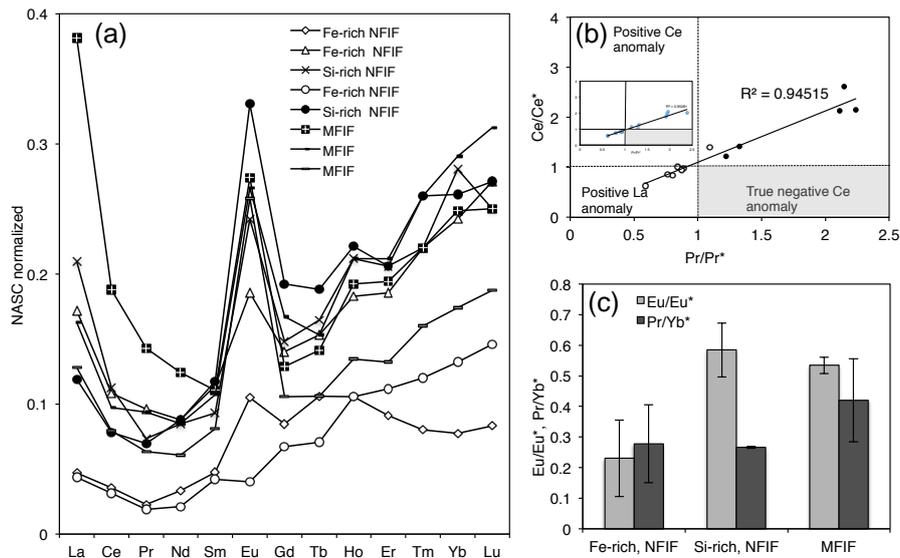
Figure 14. REE distribution in samples and calculated Ce and Eu anomalies for NFIF bands and MFIF. **(a)** NASC normalized REE distribution in various rock facies. **(b)** Ce anomalies. **(c)** Eu anomalies and light REE (LREE) vs. heavy REE (HREE) ratio in the NFIF bands and MFIF. Similar trends were reproduced for PAAS normalized REE (McLennan, 1989; Bau and Dulski, 1986), exemplified by the inset in **(b)**.

normalization protocol effectively captures the redox depositional conditions of the Milos IF.

3.4 Lipid biomarker distribution and chemotaxonomy

Bulk $\delta^{13}C_{org}$ averaged $-25.4‰$ (SD: ± 0.22) and $-25.2‰$ (± 0.26) for NFIF Fe- and Si-rich bands, respectively, and $-25.6‰$ (SD: ± 0.12) for bulk MFIF (Table 2). A fractionation effect between the alternating Fe- or Si-rich layers ($\Delta^{13}C_{\text{Fe-rich NFIF-Si-rich NFIF}}$) is estimated to be $\sim 0.23‰$ (SD: ± 0.036), while $\Delta^{13}C_{\text{Fe-rich NFIF-MFIF}}$ and $\Delta^{13}C_{\text{Si-rich NFIF-bulk MFIF}}$ is $0.13‰$ (SD: ± 0.11) and $0.36‰$ (SD: ± 0.14), respectively. These differences are small and within the margin of error of the analysis, suggesting no strong distinction in $\delta^{13}C_{org}$ preserved in the different IFs and their various facies. They are interpreted as meaning that similar carbon fixation processes operated during intervals of predominant Si and Fe(III)(oxyhydr)oxides deposition in both IFs. Attempts to discriminate between these environments by lipid biomarker analysis revealed mainly C_{16}–C_{19} fatty acid methyl esters (FAMEs) in the Fe-rich NFIF bands and in bulk MFIF, while the Si-rich NFIF bands contain mainly C_{12}–C_{21} FAMEs, suggesting either selective preservation (lipid recovery was lower in the Fe-rich MFIF bands) or shifts to different potential biological populations during the deposition of the different layers. Preserved lipids discriminate against typical microbial lipid biomarkers like hopanoids, while C3 plant FAMEs are detected in all studied materials (Fig. 15). However, the anaerobic bacteria indicator, $10MeC_{16:0}$ FAME, was identified in a few bands.

4 Discussion

4.1 Sedimentological processes

The three subbasin division of the CVSB is consistent with previous proposals suggesting that sedimentation within the CVSB was characterized by active synvolcanic rifting which must have been important in shaping basin topography and the creation of subbasin architecture (Papanikolaou et al., 1990; Stewart and McPhie, 2006; Liakopoulos et al., 2001; Papavassiliou et al., 2017). Moreover, this tectonic regime would suggest that the location(s) of volcanism were continually changing relative to the two stratigraphic sections, which themselves were also being affected, i.e., changes in depositional water depth and sedimentation style, and/or that local submarine or subaerial topographic highs impeded the lateral continuity of sedimentary units (Stewart and McPhie, 2006). Chi Fru et al. (2015) have suggested there is an upward deepening of the overall depositional setting recorded in the Little Vani section, consistent with rifting during the CVSB infilling time.

The CVSB floored by dacitic–andesitic lava domes and overlain by vocaniclastic infill, dates back to the upper Pliocene-lower Pleistocene. A complex mosaic of lithologically diverse sedimentary units (blocks), confined by neotectonic marginal faults, characterizes the CVSB (Fig. 2). The most pronounced of these faults is the NW-trending Vromolimni–Kondaros fault (Papanikolaou et al., 1990) that has been proposed as the trigger of the hydrothermal activity that deposited Mn ore in the CVSB (Papanikolaou et al., 1990; Liakopoulos et al., 2001; Alfieris et al., 2013; Papavassiliou et al., 2017). The stratigraphically tight coupling between Mn and Fe deposition, linked by Fe oxide minerals in feeder veins and positive Eu anomalies (Fig. 14) indicating vent-sourced Fe (Maynard, 2010), associates Fe mineralization with fault-triggered hydrothermalism in the CVSB. This is consistent with models of geothermal fluid circulation along fault lines as conduits for the Mn-rich fluids that formed the Milos Mn ore deposit (Hein et al., 2000; Liakopoulos et al., 2001; Glasby et al., 2005; Kilias, 2011; Papavassiliou et al., 2017). More importantly, the overall complex neotectonic structure of the CVSB (Papanikolaou et al., 1990) would explain the creation of restricted basins, with sedimentological, lithological, and geothermal conditions that enabled the development of unique biogeochemical circumstances in which the NFIF and MFIF formed.

The presence of the three depositional basins is supported by the fact that the sequence lithologies in each fault-bound unit are characterized exclusively by occurrences of specific and variably thick stratigraphic packages that tend to be absent in others. For example, the MFIF occurs restricted to Basin 1 and the NFIF to Basin 3. Basin 2 is further distinguished by 35–50 m thick interbedded ore-grade Mn-mineralized and glauconitic sandstones and sandy tuffs, much less developed in Basins 1 and 3 (Fig. 2). The presence or absence of a stratigraphic sequence, together with its thickness variation, are interpreted as a result of local syntectonic sediment formation conditions in each basin as a result of block tectonic movements along fault lines (Papanikolaou et al., 1990). It may also be attributed to unique basin-scale water column redox conditions (e.g., Bekker et al., 2010, and references therein), post-depositional erosion, and changing sea level stand (Cattaneo and Steel, 2003).

The lack of hydrothermal feeder veins or seafloor exhalative structures (i.e., chimneys) in the MFIF and NFIF lithologies suggests that hydrothermal Fe(II) was delivered by diffuse flow and that the Milos-IF formed on the seafloor. Further, mineralization of the MFIF is suggested to have occurred during two major hydrothermal venting stages. The first produced the MFIF and the second contaminated it with cryptomelane. Cryptomelane in the MFIF is therefore not a replacement product of primary Mn oxides formed during the deposition of the MFIF because the anoxia prevailing in Basin 1 at the time (Figs. 2 and 13c) would have precluded the precipitation of Mn oxide minerals, hinting that a second-phase hydrothermal fluid emission rich in dissolved Mn directly precipitated cryptomelane from solution as a secondary mineral relative to the primary Fe(III)(oxyhydr)oxides in the MFIF. This occurred during an
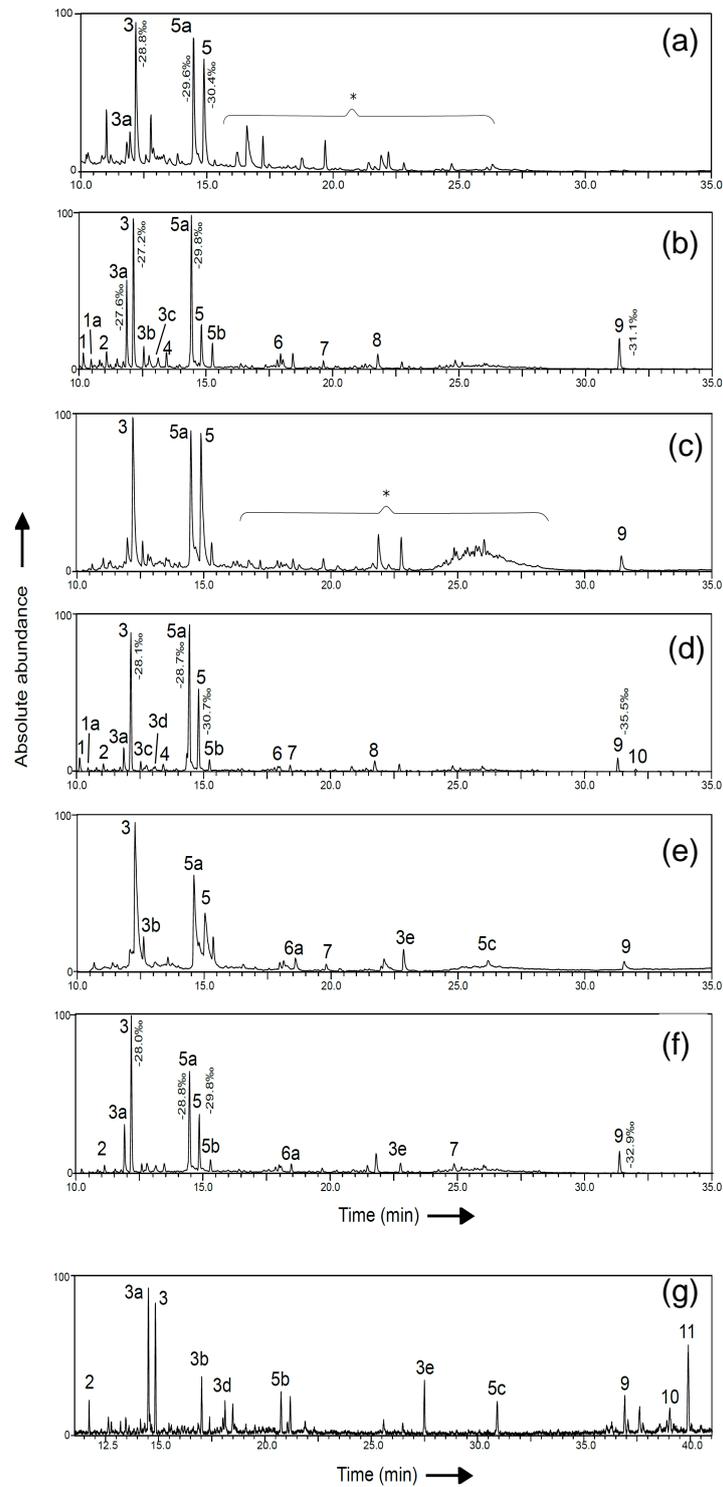
Figure 15. GC/MS chromatogram sections of total lipid extracts of the BIF-type rocks (**a–f**). Data are for individual bands excised from the sawn rock in Fig. 7e. Panel (**g**) illustrates total lipid extract for the modern shallow submarine hydrothermal sediments at Spathi Bay, on the southeast coast of Milos Island. Peak values indicate the lipid-specific $\delta^{13}C$ values per mil. Because of the low intensity of the lipids recovered, it was not possible to obtain $\delta^{13}C$ values specific for all peaks. Peaks are annotated as FAME – fatty acid methyl ester; Me – methyl group; TMS – trimethylsilyl; TMSE – trimethylsilyl ester. (1) $C_{14:0}$ FAME; (1a) $C_{14:0}$ 13Me FAME; (2) $C_{15:0}$ FAME; (3) $C_{16:0}$ FAME; (3a) $C_{16:9}$ FAME; (3b) C16 : 0 TMS; (3c) 10Me $C_{16:0}$ FAME; (3d) $C_{16:9}$ FAME; (3e) $C_{16:0}$ TMSE; (4) $C_{17:0}$ TMS; (5) $C_{18:0}$ FAME; (5a) $C_{18:9}$ FAME; (5b) $C_{18:0}$ TMS; (5c) $C_{18:0}$ TMSE; (6) $C_{19:0}$ FAME; (6a) $C_{19:0}$ 18Me TMS; (7) $C_{21:0}$ TMS; (8) $C_{22:0}$ TMS; (9) cholesterol TMS; (10) stigmasterol TMS; (11) beta-sitosterol (*) contaminants (e.g., phthalates).

episode when the MFIF deposit must have been exposed to oxygenated fluids, most likely through mixing with seawater at depth, indicated by the abundance of cryptomelane at the base of the MFIF. Our model for cryptomelane precipitation in the MFIF is therefore different from the one suggesting diagenetic transformation of primary Mn ores at Milos (Hein et al., 2001; Liakopoulous et al., 2001; Papavassiliou et al., 2017).

Geomorphological and chemical reconfiguration orchestrated the deposition of the NFIF in a deeper, small, restricted basin (Fig. 2). The deepening of Basin 3 is reflected in the underlying graded conglomerate bed that exhibits an upward fining trend, followed by transition into the fine-grain NFIF. The conglomerate bed may represent rapid deposition during a high-energy event, i.e., storm or mass flow, whereas the upward fining in the bed is better explained by the depositional mechanism losing energy through time. These high-energy conditions must have ceased during the deposition of the overlying NFIF, where we interpret that increased abundance of finely laminated IF and decreased evidence of storm and/or mass flow reworking reflects deepening conditions. The hypothesized deepening of Basin 3 is consistent with the interpretation that active rifting was an important mechanism in the formation of the CVSB (Papanikolaou et al., 1990).

4.2 Formation mechanism of the Milos BIF$_S$

4.2.1 Paragenetic sequence

It is stressed that the previously generalized model proposed for biological deposition of the Milos IF refers exclusively to parts of what is here designated as MFIF (Chi Fru et al., 2013). The NFIF is banded but does not display the typical microfossils seen in the MFIF, where diffused microbanding apparently relates to the distribution of microbial mats in thin sections (Chi Fru et al., 2013, 2015). The distinction of microcrystalline quartz and amorphous silica phases in the MFIF and NFIF, respectively, together with nanocrystalline hematite particles, suggests a primary amorphous silica origin in both deposits, diagenetically transformed to quartz in the MFIF. The difference in silica crystallinity between the IFs is concurrent with the older age predicted for the MFIF relative to the NFIF, from reconstructed sequence stratigraphy (Fig. 2). Hematite in BIFs is generally interpreted, based on thermodynamic stability, to be a transformation product of various primary Fe(III) minerals, with ferrihydrite often proposed as the primary water column precipitate (Glasby and Schulz, 1999; Bekker et al., 2010; Johnson et al., 2008; Percoits et al., 2009). It is thought that acidic pH yields mainly goethite while hematite is produced at circumneutral pH (Schwertmann and Murad, 1983). The notable absence of diagenetic magnetite and Fe carbonates (siderite and ankerite) points to negligible coupling of primary Fe(III) oxyhydroxide reduction to organic-matter oxidation by the dissimilatory iron-reducing bacteria during burial diagenesis (Johnson

et al., 2008). The minor occurrence of iron-silicate phases (Chi Fru et al., 2015) indicates an origin of the hematite precursor in seawater independent of the iron silicate proposed in some cases (Fischer and Knoll, 2009; Rasmussen et al., 2013, 2014). The Fe content of up to 50 wt % recorded in the Fe-rich bands indicates that large amounts of dissolved Fe(II) were intermittently sourced and deposited as primary Fe(III) minerals, through various oxidative processes in the depositional basin.

Importantly, the CIA analysis does not support mass weathering and mineralization of terrestrial Fe and Si, in agreement with the absence of rivers draining into the CVSB (Chi Fru et al., 2013). The specific identification of plant biolipids would at face value imply post-depositional contamination. However, samples were sawn to remove exposed layers, and only the laminated bands for the NFIF were analyzed. Modern sediments from Spathi Bay, located in the southeast of Milos Island, where hydrothermal activity presently occurs at 12.5 m below sea level, revealed similar plant lipids as recorded in the Quaternary IF (Fig. 15g). Post-depositional contamination with terrestrial plant lipids is therefore ruled out for the idea that recalcitrant plant biomass probably entered the sediments via seawater entrainment at the time of deposition. This finding necessitates the careful interpretation of bulk $\delta^{13}C_{org}$ values obtained from both the modern and ancient Milos sediments, involving in situ and ex situ biological contributions to $^{13}C_{org}$ fractionation by various known carbon fixation pathways (Preuß et al., 1989; Berg et al., 2010).

4.2.2 Tectono-sedimentary processes and band formation

Fluctuation in hydrothermal activity is proposed to account for the banding in the NFIF (Fig. 16) under redox depositional conditions inferred to be mainly reducing for both investigated IFs, consistent with previous reports (Chi Fru et al., 2013, 2015). Positive Eu anomalies indicate a hydrothermal origin for all but one of the sample suites (Fig. 14a). However, statistically calculated Eu / Eu* anomalies ($Eu_{(SN)}/(0.66Sm_{(SN)}+0.33Tb_{(SN)})$) to correct for differences in Gd anomalies commonly encountered in seawater (Planavsky et al., 2010) are in the range of 0.1–0.58, averaging 0.42. The lack of statistically significant true negative Ce anomalies (Fig. 14b) supported by sequential Fe redox reconstruction (Fig. 3c, d; Planavsky et al., 2010; Poulton and Canfield, 2005, 2011; Guilbaud et al., 2015; Sperling et al., 2015) indicates a reducing depositional environment for both the MFIF and the NFIF.

CIA analyses traditionally provide relative information on contributions from chemical weathering to sediment deposition, linked to operative hydrological and climatological patterns on land. This information is often gleaned from ancient and modern soils and from reworked siliciclastic deposits in marine basins (Maynard, 1993; Bahlburg and Dobrzin-
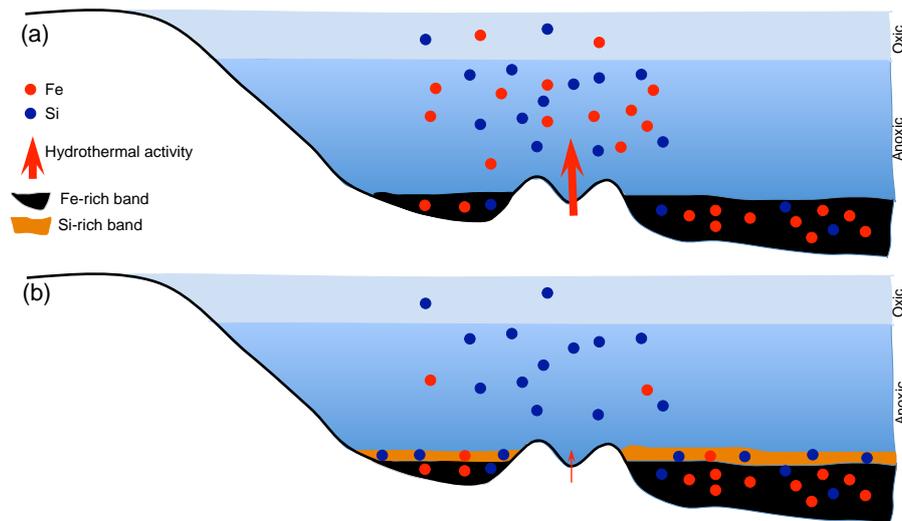
Figure 16. Conceptual model for band formation of the NFIF, related to changes in the intensity of hydrothermal activity and chemical oxidation of Fe(II) to Fe(III) in the water column, inferred from the data. See Chi Fru et al. (2013) for a biological model for the formation of the MFIF.

ski, 2011). The calculated CIA values, however, are closer to the range obtained for unweathered and/or only minimally weathered volcanic rocks (e.g., Nesbitt and Young, 1982; Bahlburg and Dobrzinski, 2011), thus pointing to a predominantly volcanic and/or hydrothermal provenance for the clastic sedimentary materials in the IFs.

It has been suggested that the release of reduced submarine hydrothermal fluids contributed to maintaining water column anoxia during the deposition of Precambrian BIFs (Bekker et al., 2010). The calculated Eu anomalies (Fig. 14) and petrographic data showing volcaniclastic detritus (i.e., K-feldspar, sanidine, tridymite, cristobalite) as key rock components are in agreement with a submarine hydrothermal source for the investigated IFs. The coarse volcaniclastic detritus embedded in the Fe-rich bands compared to the finer particles in the Si-rich layers, highlights rapid oxidation of Fe(II) that coincided with periodic cycles of hydrothermal and volcanic discharge of new materials into the water column. However, the fine-grained nature of both the MFIF and NFIF deposits suggests that deposition likely occurred away from where such activity was occurring or that volcanic and hydrothermal discharge of Fe and Si was noneruptive and disruptive. The Fe-rich bands repetitively revealed hematite grains cementing the denser volcaniclastic fragments that gradually diminish upwards into a zone of fine-grained hematite before transitioning into Si-rich bands consisting mainly of finer volcaniclastic detritus. These observations provide three valuable interpretational considerations for proposing a model for the formation of the alternating Si- and Fe-rich bands.

The Si- and Fe-oxide-rich bands are primary precipitates formed in the water column, by a process in which the precipitation of amorphous Si occurred during quiescent non-

volcanic intervals, with the oxidation and precipitation of reduced Fe intermittently introduced into the water column by volcanic and hydrothermal activity to form the Fe oxides.

The repetitive zonation of distinct particle sizes suggests density gradient sedimentation that requires a water column-like environment rather than diagenetic alteration of preformed sediments by hydrothermal fluids.

The reducing depositional conditions do not support sediment diagenesis as an alternative model for explaining the origin of the Milos IF. This is because the oxidation of ferrous Fe supplied in reduced hydrothermal fluids, must interact with a sizeable pool of oxygen, enabling microaerophilic bacterial oxidation of ferrous iron to Fe(III)(oxyhydr)oxides (Johnson et al., 2008; Chi Fru et al., 2012). Otherwise, light-controlled photoferrotrophy oxidizes ferrous Fe to form ferric (oxyhydr)oxides in the absence of oxygen in the photic zone of the water column (Weber et al., 2006).

4.2.3 Biological involvement

Hematite precipitation in the MFIF on microbial filaments (Chi Fru et al., 2013) was previously used to propose a generalized basin-scale mechanism for the deposition of Fe-rich rocks in Cape Vani. However, such filaments are absent in the NFIF, while pure hematite grains are tightly bound to relics of an organic-matter signal carrying a maximum $\delta^{13}C_{org}$ signature of $-25\%_o$ (Table 2). Similar processes are recorded in modern marine sediments where interactions between Fe and free organic matter have been reported to enable the preservation of up to 21.5 wt % of total organic carbon over geological timescales (Lalonde et al., 2012). Moreover, Fe generally traps and preserves organic matter at redox interfaces (Riedel et al., 2013). The data appear to suggest that the mechanism

of Fe(III) (oxyhydr)oxide precipitation and preservation varied between the two IFs. The photoferrotrophic-like filamentous fossils reported in the MFIF (Chi Fru et al., 2013) are absent in the NFIF. This does not, however, rule out the potential role of microbial involvement in Fe(II) oxidation, as diverse microbial taxa carry out this process, several of which are nonfilamentous (Chi Fru et al., 2012). However, our data are insufficient to enable a clear quantification of the levels of abiotic vs. biotic contribution to Fe(II) oxidation in the NFIF. Nevertheless, the inferred predominantly anoxic depositional conditions as explained above, together with the identification of anaerobic bacteria biomarkers in the laminated bands, intuitively favor a significant contribution of anaerobic biological Fe(II) oxidation in the precipitation of primary Fe(III)(oxyhydr)oxides in the NFIF. See Weber et al. (2006) for a review of potential biological pathways to anaerobic Fe(II) oxidation.

Briefly, anaerobic microbial Fe(II) oxidation can proceed via nitrate reduction and by photoferrotrophy to deposit Fe(III)(oxyhydr)oxides. These mechanisms have been linked to microbial contribution to BIF formation (Weber et al., 2006; Kappler et al., 2005) and also to the MFIF (Chi Fru et al., 2013). However, it is also possible that microaerophilic neutrophilic Fe(II)-oxidizing bacteria likely played an important role, assuming a depositional setting analogous to the Santorini caldera and Kolumbo shallow submarine volcanoes, where such low-O_2-dependent microbial Fe(II) oxidation has been identified to actively precipitate Fe(III)(oxyhydr)oxides (Kilias et al., 2013b; Camilli et al., 2015). It appears that in the MFIF, precipitating Fe(III)(oxyhydr)oxide minerals were bound and preserved free of organic carbon or that such organic carbon was diagenetically degraded. As was previously shown, Fe(III)(oxyhydr)oxides completely replaced the organic content of the filamentous microfossils in the MFIF (Chi Fru et al., 2013).

The $10MeC_{16:0}$ FAME identified in the rocks has been reported in anaerobic organisms coupling nitrite reduction to methane oxidation (Kool et al., 2012) in sulfate and iron-reducing bacterial species such as *Desulfobacter*, *Desulfobacula* (Bühring et al., 2005; Dowling et al., 1986; Taylor and Parkes, 1983), *Geobacter*, *Marinobacter*, and the marine denitrifier, *Pseudomonas nautical* (Bühring et al., 2005; Dowling et al., 1986). It had previously been proposed that post-depositional denitrification was a potential pathway for early organic-matter removal, justified by the low rock organic carbon and nitrogen content in the Milos BIF-type rocks (Chi Fru et al., 2013, 2015; Table 2). Equally, the detected $10MeC_{16:0}$ FAME has also been found in anaerobic oxidation of methane (AOM) communities (Alain et al., 2006; Blumenberg et al., 2004), originating from sulfate-reducing bacteria. However, bulk sediment $\delta^{13}C_{org}$ of $-20\permil$ does not reflect AOM activity that is expected to produce bulk $\delta^{13}C_{org}$ values that are $\leq -30\permil$. Low $10MeC_{16:0}$ FAME concentrations frustrated attempts at ac-

quiring its compound-specific isotopic signature to enable further biomolecular-level reconstruction of active microbial metabolisms to explain Fe deposition mechanisms.

It is nevertheless puzzling why potential microbial biomarkers typical of marine or hydrothermal vent environments are hardly preserved in the rocks, given that microfossil evidence indicates a vast community of diverse prokaryotic assemblages in the adjacent MFIF (Chi Fru et al., 2013, 2015). Moreover, sediments of the modern Milos hydrothermal system and elsewhere on the HVA are ubiquitously colonized by microbial life, characterized by the marked large-scale absence or low abundance of higher life forms, including plants (Kilias et al., 2013b; Camilli et al., 2015; Oulas et al., 2016). One possibility could be the discriminatory preservation of lipids related to their selectivity and reactivity towards Fe(III)(oxyhydr)oxides and clays or different pathways to diagenetic degradation (e.g., Canuel and Martens, 1996; Lü et al., 2010; Riedel et al., 2013). As noted, the carbonaceous materials in the BIF-type NFIF rocks occur in tight association with hematite.

Importantly, prokaryotic biomarkers are suggested to poorly preserved in these young BIF analogs. This raises the possibility that this may provide an important explanation for why lipid biomarkers are yet to be extracted from Precambrian BIFs. Moreover, the data are compatible with the low C_{org} recorded in BIFs of all ages, suggesting that the low C_{org} abundance may not be due to metamorphism as often proposed (Bekker et al., 2010) or to C_{org} oxidation by dissimilatory iron-reducing bacteria to form ^{13}C-depleted siderite and ankerite during diagenesis (Johnson et al., 2008; Bekker et al., 2010). The Milos BIF-type rocks are unmetamorphosed and lack iron carbonate, yet have vanishingly low C_{org} levels similar to the ancient metamorphosed BIFs. However, an alternative possibility is that the iron oxides may have been reduced through biological oxidation of organic carbon, but carbonate saturation was not reached (Smith et al., 2013).

4.2.4 Mn layers and the deposition of the Si- and Fe-rich facies

Cryptomelane ($K(Mn^{4+}, Mn^{2+})_8O_{16}$), which commonly occurs in oxidized Mn deposits resulting from mineral replacement and as open-space fillings (Papavassiliou et al., 2016), is also common in the MFIF. This supports the idea of post-depositional impregnation of the base of the MFIF by Mn-rich fluids. Microscopic analysis supports the epigenetic origin of the Mn in the MFIF by revealing Mn oxides growing along fractures, impregnating and replacing Fe minerals (Fig. 4b–f). The macroscopically evident thinning out and disappearance of such Mn-rich horizons up the MFIF, coupled by their development along microfractures emphasizes this epigenetic origin. Mn is not a common feature of the NFIF, even though it sits on top of a thin sandstone layer that is highly mineralized with Mn, locally forming the cap of the main Mn ore at Cape Vani. The generally accepted view

is that Mn-rich hydrothermal fluids rose and mineralized the Cape Vani sandstones (Hein et al., 2000; Liakopoulos et al., 2001; Glasby et al., 2005). Based on the stratigraphic location of the MFIF, which predates the Mn-rich sandstones, it is proposed that impregnation of the MFIF by Mn was coeval with large-scale Mn ore mineralization of the Cape Vani sandstones, implying the entire basin was likely oxygenated at the time. The lack of Ce anomalies, confirmed by the sequential Fe extraction proxy data, suggests that both the MFIF and the NFIF formed in anoxic settings. Similar data for the Mn oxides have suggested formation in oxic settings (Glasby et al., 2005; Chi Fru et al., 2015). This implies that Mn epigenetically replaced the MFIF, either because the basin was tectonically uplifted into a high-energy oxygenated shallow-water setting or that the sea level dropped, leading to partial metasomatism of the base of MFIF, when oxygenated seawater mixed with reduced hydrothermal fluids and precipitated Mn. The lack of significant Ce anomalies in the dataset, combined with the inferred deepening of Basin 3 and the anoxic depositional conditions suggested by the sequential iron redox proxy, further indicates that for the final deposition of the NFIF, an eventual deepening event must have been triggered, resulting in deoxygenation of parts of the CVSB.

All of this is feasible with the three-basin fault-bounded hypothesis as a requirement for movement along fault lines in response to temporal tectonic activation. The upward sequence transition from the Mn-rich sandstone facies, through the pebbly conglomerate and the final termination in the overlying mud-grained NFIF (Fig. 8b), reflects sedimentary features formed during multiple changes in seawater levels (Cattaneo and Steel, 2000).

Uplifting is suggested by potential weathering of the NFIF to form the ferruginous duricrust cap. Comparable ferruginous layers on Precambrian BIFs are linked to pervasive subaerial chemical weathering, via the dissolution of the silica-rich layers and precipitation of relatively stable Fe oxides in the spaces between more resistant hematite crystals (e.g., Dorr, 1964; Shuster et al., 2012; Levett et al., 2016). This collective evidence supports the existence of a geodynamic tectonic system capable of producing shallow oxic to deeper anoxic basin conditions at different times that would explain the existence of Mn and Fe oxide layers within the same sedimentary sequence. For example, it is common knowledge that both Fe and Mn oxides will precipitate in the presence of oxygen (Roy, 1997, 2006), with kinetic rates usually being faster for the oxidation of reduced Fe than reduced Mn. In the Fe(II)-rich conditions that prevail in anoxic settings, abiotic reactions between Fe(II) and Mn oxides, produce Fe(III) leading to the dissolution of the Mn oxides to form reduced Mn, implying Mn oxides should not accumulate (Dieke, 1985). Moreover, under these conditions, biological precipitation of Fe(III) can occur rapidly, leaving dissolved Mn in solution to be deposited when oxygen becomes available. Given that the hydrothermal fluids of the Hellenic

Volcanic Arc are commonly enriched in both reduced Fe and Mn, the deposition of the MFIF and NFIF therefore implies there was an existing mechanism that enabled the kinetic discrimination and deposition of the oxides of Fe and Mn into separate settings, most likely dependent on prevailing redox conditions. The accumulation of the ferruginous duricrust layer, overprinted by redox sensitive Mn nodules, above the NFIF indicates a new shallowing event might have terminated the formation of the NFIF.

4.2.5 Modern analogs on the HVA

A mechanistic explanation for the development of potential stratified waters and reducing conditions during the deposition of the Milos BIF is problematic. However, evidence is available from present shallow submarine hydrothermal analogs in the central part of the HVA, to which the CVSB belongs. These include

1. the crater floor of the Kolumbo shallow submarine volcano ($\sim 600 \times 1200$ m), which rises 504 m from the crater floor to 18 m b.s.l. (Sigurdsson et al., 2006; Kilias et al., 2013b)

2. the N part of Santorini's submerged caldera walls, which rises from 390 m b.s.l. to over 300 m a.s.l. (Druitt et al., 1999; Friedrich et al., 2006; Nomikou et al., 2013; Camilli et al., 2015)

3. the coastal embayments at the Kameni emergent volcanic islands in the center of the Santorini caldera (Hanert, 2002; Nomikou et al., 2014; Robbins et al., 2016).

The benthic waters within Kolumbo's crater potentially sustain O_2-depleted conditions via stable CO_2-induced water column densification, and accumulation of acidic water (pH ~ 5), extending ~ 10 m above the CO_2 venting crater floor (Kilias et al., 2013b). This phenomenon is believed to lead not only to the obstruction of vertical mixing of bottom acidic water but also to O_2 deprivation by precluding the efficient transfer of oxygenated surface seawater into the deeper crater layer. In addition, diffuse CO_2 degassing is believed to be linked to the formation of Fe microbial mats and amorphous Fe(III) oxyhydroxides on the entire Kolumbo crater floor (Kilias et al., 2013b) and on the shores of Milos Island (Callac et al., 2017). Prerequisites for the O_2-depleted conditions to happen are the closed geometry of the Kolumbo crater and the virtually pure CO_2 composition of the released hydrothermal vent fluids that produce O_2 stratification along a stable CO_2 pH gradient.

A similar scenario is reported for the Santorini caldera, where large (~ 5 m diameter) CO_2-rich, acidic (pH ~ 5.93) hydrothermal seafloor pools and flow channels develop within meter-thick microbial Fe-mats on the seafloor slope at 250–230 m below sea level. Persistent hypoxia exists in these pools, representing concentrated seafloor CO_2 accumulation centers generated by hydrothermal venting (Camilli

et al., 2015). Here, the dissolved O_2 content ($\sim 80\,\mu M$ or less) in the pools is $\sim 40\,\%$ depleted relative to the surrounding ambient seawater (Camilli et al., 2015). These hypoxic conditions are comparable to or even lower than those measured in the CO_2-rich oxygen minimum zones of coastal oceans, relative to seawater existing in equilibrium with atmospheric pO_2 and pCO_2 pressures (Paulmier et al., 2008, 2011; Franco et al., 2014). These conditions enable strong redox stratification of the pool waters, in which unique Si- and Fe-rich microbial mats are associated with amorphous opal and Fe(III)(oxyhydro)xides (Camilli et al., 2015). Importantly, the Fe microbial mats in these CO_2-rich hypoxic pools are affiliated with specific microaerophilic Fe(II)-oxidizing bacteria that accumulate Fe(III) oxyhydroxides (Camilli et al., 2015; Oulas et al., 2016). These Fe bacteria are implicated in the deposition of the Precambrian BIFs (Konhauser et al., 2002; Planavsky et al., 2009; Bekker et al., 2010).

Hypoxia is also associated with the water column of the Fe(III)-rich coastal embayments and their hydrothermal vents ($\leq 1.0\,m$ water depth), Kameni islands (Hanert, 2002; Robbins et al., 2016 and references therein). Venting fluids are warm (20–40 °C), acidic to circumneutral (pH 5.5–6.9) and enriched in CO_2, Fe, and Si (Georgalas and Liatsikas, 1936; Boström et al., 1990; Handley et al., 2010; Robbins et al., 2016). Water column stratification is expressed as decreasing O_2 with depth that is positively related to Fe(III)(oxyhydr)oxide density and microaerophilic Fe(II)-oxidizing bacterial prevalence (Hanert, 2002). Robbins et al. (2016) found that Fe(III)-rich suspended particulate material in these "Fe bays" may be associated with anoxia, extending up to the air–seawater interface, near the hydrothermal vents (Hanert, 2002). They consist of ferrihydrite, goethite, and microaerophilic Fe(II) oxidizers.

However, the biogeochemical occurrence of these phenomena within the localized confines of the Santorini caldera and Kolumbo crater, may however be difficult to achieve in ordinary shallow submarine hydrothermal settings, such as those occurring on the coast of present-day Milos. The same may be true for Tatum Bay, where nonvolcanic and unconfined diffuse hydrothermalism is widespread (Dando et al., 1996; Pichler and Dix, 1996; Pichler and Veizer, 1999; Stüben et al., 1999; Rancourt et al., 2001; Varnavas et al., 2005).

In the Kolumbo and Santorini hydrothermal fields, benthic pH averages 5.5 and the deposition of carbonates is markedly absent (Kilias et al., 2013b; Camilli et al., 2015; Robins et al., 2016). This conforms to observations in the MFIF and NFIF units where carbonate mineralization is not detected, thereby suggesting a similar low-pH depositional environment for both the MFIF and NFIF. Ubiquitous Fe(III)(oxyhydr)oxide precipitation and enriched Si content are prevalent in the CO_2-rich hypoxic shallow submarine Santorini caldera slope pools and the Kameni Fe embayments, where sulfide precipitation is restricted (Camilli et al., 2015; Robbins et al., 2016).

Such sulfide-poor conditions are critical for the formation of BIFs (Bekker et al., 2010).

A high Si and Fe(III)(oxyhydr)oxide content, absence of detectable carbonate and Fe sulfide minerals are hallmark characteristics of the Milos IF (Chi Fru et al., 2013, 2015; Fig. 13c, d). This depositional situation is different, for example, from the unconfined shallow submarine hydrothermal activity in Tatum Bay and Bahía Concepción, Baja California Sur state, Mexico, where authigenic carbonate deposition is widespread (Canet et al., 2005; Pichler and Veizer, 2004). Moreover, there is strong geological evidence that within volcanic crater environments associated with high CO_2 emission, long-term water column redox stratification is possible under these special conditions. For example, Lake Nyos, a 205 m deep volcanic crater lake in Cameroon, central West Africa, undergoes CO_2-induced water column stratification, lasting several decades. The reducing bottom waters contain low sulfate and elevated reduced Fe concentrations, relative to the oxidized surface water (Kling et al., 2005; Tiodjio et al., 2014; Ozawa et al., 2016).

5   Concluding remarks

This study shows the following new insights compared to what was previously known:

1. At least two distinct IFs (MFIF and NFIF) formed from hydrothermal mud, within two localized subbasins in the $\sim 1\,km$ long CVSB, ~ 2.66–$1.0\,Myr$ ago, controlled by local tectonism.

2. Local conditions of elevated and cyclic supply of ferrous Fe and dissolved Si, accompanied by bottom water anoxic conditions in a localized reservoir cut off from the open ocean, can in principle allow the deposition of BIF-type rocks in a modern marine setting. The rarity of this type of deposit, however, suggests that the conditions required for formation are not a frequent occurrence under the present-day oxygen-rich atmosphere.

3. A working model that band formation may involve potential Fe(III)(oxyhydr)oxide infilling of sediment pores and fractures during diagenesis is not supported by the data. In addition to the lack of observation of such phenomena, as shown for replacive Mn mineralization, calculated Ce, and Eu anomalies, together with sequential iron extraction analysis, are suggestive of anoxic depositional conditions likely induced by the release of reduced hydrothermal and volcanic fluids into a cutoff sedimentary basin.

4. Both Fe(III)(oxyhydr)oxides and Mn oxides are precipitated in the presence of oxygen. In its absence, the formation of Mn oxides is inhibited, while photoferrotrophy in the anoxic photic zone of redox-stratified waters oxidizes reduced Fe to Fe(III)(oxyhydr)oxides (Kappler

et al., 2005; Weber et al., 2006). Collectively, these observations provide an important feasible mechanism for the razor-sharp separation of the Mn-oxide-rich ores in the CVSB, which are also Fe(III)(oxyhydr)oxide rich, from the highly localized MFIF and NFIF deposits that are Fe(III)(oxyhydr)oxide-rich but Mn-oxide-poor.

5. The mechanism of formation of the MFIF and NFIF, therefore, most likely involved an exhalative release of reduced hydrothermal and volcanic fluids into a restricted and deoxygenated seafloor water column where the oxidation of reduced Fe to Fe(III)(oxyhydr)oxides occurred, most likely by the activity of photoferrotrophs (Chi Fru et al., 2013). Microaerophilic oxidation of Fe(II) was likely critical but that remains to be explored.

6. Episodic intensification of hydrothermal activity is identified as a main mechanism for the formation of the millimetric BIF bands, adding to the biological mechanism that was inferred from fossil records in the MFIF (Chi Fru et al., 2013, 2015).

7. Abiotic Si precipitation was much slower relative to Fe(III) precipitation, resulting in Fe-rich bands in the NFIF forming in association with large fragments of volcaniclast and the Si-rich bands with finer Si grains.

8. A combination of the above processes produced pulses of Si and Fe in the millimetric Si- and Fe-rich bands in the NFIF.

9. Whether the rocks described here are analogs of Precambrian BIFs or not, and whether the proposed formation mechanisms match those that formed the ancient rocks, is open to debate. However, there are many similarities to proposed Precambrian BIF depositional models (e.g., Klein, 2005; Beukes and Gutzmer, 2008; Smith et al., 2013; Bekker et al., 2010; Klein and Beukes, 1992). Importantly, the present study provides mechanisms by which rocks with alternating Fe and Si-rich bands can be formed in the modern ocean.

The Supplement related to this article is available online at https://doi.org/10.5194/se-9-573-2018-supplement.

References

Alain, K., Holler, T., Musat, F., Elvert, M., Treude, T., and Kruger M.: Microbiological investigation of methane- and hydrocarbon-discharging mud volcanoes in the Carpathian Mountains, Romania, Environ. Microbiol., 8, 574–590, 2006.

Alfieris, D.: Geological, geochemical and mineralogical studies of shallow submarine epithermal mineralization in an emergent volcanic edifice, at Milos Island (western side), Greece, PhD thesis, Department of Geosciences at Universität Hamburg, 2006.

Alfieris, D. and Voudouris, P.: Ore mineralogy of transitional submarine magnatic-hydrothermal deposits in W. Milos Island, Greece, Bulg. Acad. Sci., 43, 1–6, 2005.

Alfieris, D., Voudouris, P., and Spry, P.: Shallow submarine epithermal Pb–Zn–Cu–Au–Ag–Te mineralization on western Milos Island, Aegean Volcanic Arc, Greece: Mineralogical, geological and geochemical constraints, Ore Geol. Rev., 53, 159–180, 2013.

Anand, R. R., Paine, M., and Smith, R. E.: Genesis, Classification and Atlas of Ferruginous Materials, Yilgarn Craton, CRC LEME Open File Report, vol. 13, CSIRO Exploration and Mining, Perth, 2002.

Bahlburg, H. and Dobrzinski, N.: A review of the Chemical Index of Alteration (CIA) and its application to the study of Neoproterozoic glacial deposits and climate transition, Geol. Soc. London Mem., 36, 81–92, 2011.

Bau, M. and Dulski, P.: Distribution of yttrium and rare- earth elements in the Penge and Kuruman Iron-Formations, oxidative scavenging of cerium on hydrous Fe oxide, Transvaal Supergroup, South Africa, Precambrian Res., 79, 37–55, 1996.

Berg, I. A., Kockelkorn, D., Ramos-Vera, W. H., Say, R. F., Zarzycki, J., Hügler, M., Alber, B. E., and Fuchs, G.: Autotrophic carbon fixation in archaea, Nat. Rev. Microbiol., 8, 447–460, 2010.

Bekker, A., Slack, J. F., Planavsky, N., Krapež B., Hofmann, A., Konhauser, K. O., and Rouxel, O. J.: Iron formation: The sedimentary product of a complex interplay among mantle, tectonic, oceanic, and biospheric processes, Econ. Geol., 105, 467–508, 2010.

Beukes, N. J. and Gutzmer, J.: Origin and Paleoenvironmental significance of major Iron Formations at the Archean-Paleoproterozoic boundary, Econ. Geol. 15, 5–47, 2008.

Beukes, N. J., Swindell, E. P. W., and Wabo, H.: Manganese deposits of Africa, Episodes, 39, 285–317, 2016.

Blumenberg, M., Seifert, R., Reitner, J., Pape, T., and Michaelis, W.: Membrane lipid patterns typify distinct anaerobic methanotrophic consortia, P. Natl. Acad. Sci. USA, 101, 11111–11116, 2004.

Boström, K., Honnorez, J., Joensuu, O., and Rydell, H.: Chemistry of hydrothermal solutions in drill hole GPK-1, Palaea Kameni, Santorini, Greece, Proceedings of the third international congress, Santorini, Greece, 3, 257–260, 1990.

Bouma, A. H.: Sedimentology of Some Flysch Deposits, Amsterdam, Elsevier, 168 pp., 1962.

Bronn, H. G.: Ubersicht der Fossilen Uberreste in den tertiären subappeninischen Gebirgen, Italiens Tertiär-Gebilde und deren organische Einschlüsse, Heidelberg, XII + 176 + 1 pl, 1831.

Breitkreuz, C.: Spherulites and lithophysae – 200 years of investigation on hightemperature crystallization domains in silica-rich volcanic rocks, Bull. Volcanol., 75, 1–16, 2013.

Bühring, S. I., Elvert, M., and Witte, U.: The microbial community structure of different permeable sandy sediments characterized by the investigation of bacterial fatty acids and fluorescence in situ hybridization, Environ. Microbiol., 7, 281–293, 2005.

Callac, N., Posth, N. R., Rattray, J. E., Yamoah, K. K. Y., Wiech, A., Ivarsson, M., Hemmingsson, C., Kilias, S. P., Argyraki, A., Broman, C., Skogby, H., Smittenberg, R. H., and Chi Fru, E.: Modes of carbon fixation in an arsenic and CO_2-rich shallow hydrothermal ecosystem, Sci. Rep.-UK, 7, 14708, https://doi.org/10.1038/s41598-017-13910-2, 2017.

Camilli, R., Noumikou P., Escartin, J., Ridao, P., Mallios, A., Kilias, S. P., Argyraki, A., and the Caldera Science Team: The Kallisti Limnes, carbon dioxide accumulating subsea pools, Sci. Rep.-UK, 5, 12152, https://doi.org/10.1038/srep12152, 2015.

Canet, C., Prol-Ledesma, R. M., Torres-Alvarado, I., Gilg, H. A., Villanueva, R. E., and Cruz, R. L. S.: Silica-carbonate stromatolites related to coastal hydrothennal venting in Bahia Concepcion, Baja California Sur, Mexico, Sed. Geol., 174, 97–113, 2005.

Canuel, E. A. and Marten, C. S.: Reactivity of recently deposited organic matter: Degradation of lipid compounds near the sediment-water interface, Geochim. Cosmochim. Ac., 60, 1793–1806, 1996.

Cattaneo, A. and Steel, R. J.: Transgressive deposits: a review of their variability, Earth Sci. Rev., 62, 187–228, 2003.

Chi Fru, E., Piccinelli, P., and Fortin, D.: Insights into the global microbial community structure associated with iron oxyhydroxide minerals deposited in the aerobic biogeosphere, Geomicrobiol. J., 29, 587–610, 2012.

Chi Fru, E., Ivarsson, M., Kilias, S. P., Bengtson, S., Belivanova, V., Marone, F., Fortin, D., Broman, C., and Stampanoni, M.: Fossilized iron bacteria reveal a pathway to the origin banded iron formations, Nat. Commun., 4, 2050, https://doi.org/10.1038/ncomms3050, 2013.

Chi Fru, E., Ivarsson, M., Kilias, S. P., Frings, P. J., Hemmingsson, C., Broman, C., Bengtson, S. and Chatzitheodoridis, E.: Biogenicity of an Early Quaternary iron formation, Milos Island, Greece, Geobiology, 13, 225–44, 2015.

Dando, P. R., Hughes, J. A., Leahy, Y., Niven, S. J., Taylor, L. J., and Smith, C.: Gas venting rates from submarine hydrothermal areas around the island of Milos, Hellenic Volcanic Arc, Cont. Shelf Res., 15, 913–925, 1995.

Dieke, P.: Concentration of Mn and separation from Fe in sediments – I, Kinetics and stoichiometry of the reaction between birnessite and dissolved Fe(II) at 10 °C, Geochim. Cosmochim. Ac., 49, 1023–1033, 1985.

Dorr, J. V. N.: Supergene iron ores of Minas Gerais, Brazil, Econ. Geol., 59, 1203–1240, 1964.

Dowling, N. J. E., Widdel, F., and White, D. C.: Phospholipid ester-linked fatty-acid biomarkers of acetate-oxidizing sulfate-reducers and other sulfide-forming bacteria, J. Gen. Microbiol., 132, 1815–1825, 1986.

Druitt, T. H. L., Edwards, R. M., Mellors, D. M., Pyle, R. S. J., Sparks, M., Lanphere, M. D., and Barreirio, B.: Santorini Volcano, Geological Society Memoir, Geological Society of London, 19, 165 pp., 1999.

Fischer, W. W. and Knoll, A. H.: An iron shuttle for deepwater silica in Late Archean and early Paleoproterozoic iron formation, Geol. Soc. Am. Bull., 121, 222–235, 2009.

Franco, A. C.,Hernández-Ayón, J. M., Beier, E., Garçon, V., Maske, H., Paulmier, A., Färber-Lorda, J., Castro, R., and Sosa-Ávalos, R.: Air-sea CO_2 fluxes above the stratified oxygen minimum zone in the coastal region off Mexico, J. Geophy. Res., 119, 2923–2937, 2014.

Friedrich, W. L., Kromer, B., Friedrich, M., Heinemeier, J., Pfeiffer, T., and Talamo, S.: Santorini eruption radiocarbon dated to 1627–1600 BC, Science, 312, 548–548, 2006.

Fytikas, M., Innocenti, F., Kolios, N., Manetti, P., Mazzuoli, R., Poli, G., Rita, F., and Villari, L.: Volcanology and petrology of volcanic products from the island of Milos and Neighbouring islets, J. Vol. Geotherm. Res., 28, 297–317, 1986.

Galan, L. D. P., Doval, M., La Iglesia, A., Soriano, J., and Chavez, L.: Occurrence of silica polymorphs nanocrystals in tuffaceous rocks, Province of the Mesa Central, Mexico, and their formation from subcritical Si-rich fluids, Am. Mineral., 98, 977–985, 2013.

Georgalas, G. and Liatsikas, N.: Die Historische entwickelung des Dafni-Ausbruches 1925–1926, in: Santorin, Der Werdegand eines Inselvulkans und sein Ausbruch 1925–1928, edited by: Reck, H., Verlag von Dietrich Reimer, Berlin, 2, 1–96, 1936.

Glasby, G. P. and Schulz, H. D.: Eh, pH diagrams for Mn, Fe, Co, Ni, Cu and As under seawater conditions: application of two new types of the Eh, pH diagrams to the study of specific problems in marine geochemistry, Aquatic Geochem., 5, 227–248, 1999.

Glasby, G. P., Papavassiliou, C. T., Mitsis, J., and Valsami-Jones, E.: The Vani manganese deposit, Milos island, Greece: A fossil stratabound Mn−Ba−Pb−Zn−As−Sb−W-rich hydrothermal deposit, Develop. Volcanol., 7, 255–291, 2005.

Gross, G. A.: A classification of iron-formation based on depositional Environments, Can. Min., 18, 215–222, 1980.

Guilbaud, R., Poulton, S. W., Butterfield, N. J., Zhu, M., and Shields-Zou, G. A.: A global transition to ferruginous conditions during the early Neoproterozoic, Nat. Geosci., 8, 466–470, 2015.

Handley, K. M., Boothman, C., Mills, R. A., Pancost, R. D., and Lloyd, J. R.: Functional diversity of bacteria in a ferruginous hydrothermal sediment, ISME J., 4, 1193–1205, 2010.

Hanert, H. H.: Bacterial and chemical iron oxide deposition in a shallow bay on Palaea Kameni, Santorini, Greece: microscopy, electron probe microanalysis, and photometry of in situ experiments, Geomicrobiol. J., 19, 317–342, 2002.

Hein, J. R., Stamatakis, M. G., and Dowling, J. S.: Trace metal-rich Quaternary hydrothermal manganese oxide and barite deposit,

Milos Island, Greece, Applied Earth Science, Institute of Mining and Metallurgy, 109, 67–76, 2000.

Hoffman, P. F., Kaufman, A. J., Halverson, G. P., and Schrag, D. P.: A Neoproterozoic Snowball Earth, Science, 281, 1342–1346, 1998.

Horwell, C. J., le Blond, S., Michnowicz, S. A. K., and Cressey, G.: Cristobalite in a rhyolitic lava dome: evolution of ash hazard, Bull. Volcanol., 72, 249–253, 2010.

Ichihara, K. and Fukubayashi, Y.: Preparation of fatty acid methyl esters for gas-liquid chromatography, J. Lipid Res., 51, 635–40, 2010.

James, H. L.: Sedimentary facies of iron-formation, Econ. Geol., 49, 235–293, 1954.

Johnson, C. M., Beard, B. L., and Roden, E. E.: The iron isotope fingerprints of redox and biogeochemical cycling in modern and ancient Earth, Annu. Rev. Earth Pl. Sc., 36, 457–493, 2008.

Kappler, A., Pasquero, C., and Newman, D. K.: Deposition of banded iron formations by anoxygenic phototrophic Fe(II)-oxidizing bacteria, Geology, 33, 865–868, 2005.

Kilias, S. P.: Microbial mat-related structures in the Quaternary Cape Vani manganese-oxide (-barite) deposit, NW Milos island, Greece, SEPM Special Publication, 101, 97–110, 2011.

Kilias, S. P., Detsi, K., Godelitsas, A., Typas, M., Naden, J., and Marantos, Y.: Evidence of Mn-oxide biomineralization, Vani Mn deposit, Milos, Greece, in: Proceedings of the ninth biennial Meeting of the Society for Geology Applied to Mineral Deposits, Dublin, Ireland, Irish Assoc. Econ. Geol. 1069–1072, 2007.

Kilias, S. P., Chatzitheodoridis, E., and Lyon, I.: Molecular, chemical and morphological evidence for hematite biogenicity at the Quaternary Cape Vani Mn-(Ba-Fe) deposit, Milos, Greece, Bull. Geol. Soc., 47, 834–842, 2013a.

Kilias, P. S., Nomikou, P., Papanikolaou, D., Polymenakou, P. N., Godelitsas, A., Argyraki, A., Carey, S., Gamaletsos, P., Mertzimekis, T. J., Stathopoulou, E., Goettlicher, J., Steininger, R., Betzelou, K., Livanos, I., Christakis, C., Bell, K. C., and Scoullos, M.: New insights into hydrothermal vent processes in the unique shallow-submarine arc-volcano, Kolumbo (Santorini), Greece, Sci. Rep.-UK, 3, 2421, https://doi.org/10.1038/srep02421, 2013b.

Klein, C.: Some Precambrian banded iron-formations (BIFs) from around the world: Their age, geologic setting, mineralogy, metamorphism, geochemistry, and origins, Am. Min., 90, 1473–1499, 2005.

Klein, C. and Beukes, N. J.: Time distribution, stratigraphy and sedimentologic setting, and geochemistry of Precambrian Iron Formation, in: The Proterozoic Biosphere: A multidisciplinary study, edited by: Schopf, J. W. and Klein, C., Cambridge University Press, New York, 139–146, 1992.

Kling, G. W., Evans, W. C., Tanyileke, G., Kusakabe, M., Ohba, T., Yoshida, Y., and Hell, J. V.: Degassing Lakes Nyos and Monoun: Defusing certain disaster, P. Natl. Acad. Sci. USA, 102, 14185–14190, 2005.

Konhauser, K. O., Planavsky, N. J., Hardisty, D. S., Robbins, L. J., Warchola, T. J., Haugaard, R., Lalonde, S. V., Partin, C. A., Oonk, P. B. H., Tsikos, H., and Lyons, T. W.: Iron formations: A global record of Neoarchean to Palaeoproterozoic environmental history, Earth Sci. Rev., 172, 140–177, 2017.

Kool, D. M., Zhu, B., Rijpstra, W. I., Jetten, M. S., Ettwig, K. F., and Sinninghe Damsté, J. S.: Rare branched fatty acids charac-

terize the lipid composition of the intra-aerobic methane oxidizer "Candidatus Methylomirabilis oxyfera", Appl. Environ. Microbiol., 78, 8650–8656, 2012.

Krapež, B., Barley, M. E., and Pickard, A. L.: Hydrothermal and resedimented origins of the precursor sediments to banded iron formations: Sedimentological evidence from the early Palaeoproterozoic Brockman Supersequence of Western Australia, Sedimentology, 50, 979–1011, 2003.

Lalonde, K., Mucci, A., Quellet, A., and Gélinas, Y.: Preservation of organic matter in sediments promoted by iron, Nature, 483, 198–200, 2012.

Levett, A., Gagen, E., Shuster, J., Rintoul, L., Tobin, M., Vongsvivut, J., Bambery, K., Vasconcelos, P., and Southam, G.: Evidence of biogeochemical processes in iron duricrust formation, J. South. Am. Earth Sci., 71, 131–142, 2016.

Li, W., Czaja, A. D., Van Kranendonk, M. J., Beard, B. L., Roden, E. E., and Johnson, C. M.: An anoxic, Fe(II)-rich, U-poor ocean 3.46 billion years ago, Geochim. Cosmochim. Ac., 120, 65–79, 2013.

Liakopoulos, A., Glasby, G. P., Papavassiliou, C. T., and Boulegue, J.: Nature and origin of the Vani manganese deposit, Milos, Greece: an overview, Ore Geol. Rev., 18, 181–209, 2001.

Lü, D., Song, Q., and Wang, X.: Decomposition of algal lipids in clay-enriched marine sediment under oxic and anoxic conditions, Chin. J. Oceanogr. Limnol., 28, 131–143, 2010.

Marschik, R., Bauer, T., Hensler, A.-S., Skarpelis, N., and Hölzl, S.: Isotope Geochemistry of the Pb-Zn-Ba(-Ag-Au) Mineralization at Triades-Galana, Milos Island, Greece, Res. Geol., 60, 335–347, 2010.

Maynard, J. B.: Chemistry of modern soils as a guide to interpreting Precambrian Paleosols, J. Geol., 100, 279–289, 1993.

Maynard, J. B.: The chemistry of manganese ores through time: a signal of increasing diversity of earth-surface environments, Econ. Geol., 105, 535–552, 2010.

McLennan, S. B.: Rare earth elements in sedimentary rocks. Influence of provenance and sedimentary processes, in: Geochemistry and Mineralogyof the Rare Earth Elements, edited by: Lipin, B. R. and McKay, G. A., Mineralogical Society of America, Washington, 169–200, 1989.

Miall, A. D.: Lithofacies types and vertical profile models in braided river deposits, Can. Soc. Pet. Geol. Mem., 5, 597–604, 1978.

Miall, A. D.: Architectural element analysis: a new method of facies analysis applied to fluvial deposits, Earth Sci. Rev., 22, 261–308, 1985.

Morris, R. V., Vaniman, D. T., Blake, D. F., Gellert, R., Chipera, S. J., Rampe, E. B., Ming, D. W., Morrison, S. M., Downs, R. T., Treiman, A. H., Yen, A. S., Grotzinger, J. P., Achilles, C. N., Bristow, T. F., Crisp, J. A., Des Marais, D. J., Farmer, J. D., Fendrich, K. V., Frydenvang, J., Gradd, T. G., Morookian, J.-M., Stolper, E. M., and Schwenzer, S. P.: Silicic volcanism on Mars evidenced by tridymite in high-SiO2 sedimentary rock at Gale crater, P. Natl. Acad. Sci. USA, 113, 7071–7076, 2016.

Mutti, E.: Turbidite Sandstones, Agip Spe. Pub., 275 pp., 1992.

Nesbitt, H. W. and Young, G. M.: Early Proterozoic climates and plate motions inferred from major element chemistry of lutites, Nature, 199, 715–717, 1982.

Nomikou, P., Papanikolaou, D., Alexandri, M., Sakellariou, D., and Rousakis, G.: Submarine volcanoes along the Aegean volcanic arc, Tectonophysics, 597–598, 123–146, 2013.

Nomikou, P., Parks, M. M., Papanikolaou, D., Pyle, D. M., Mather, T. A., Carey, S., Watts, A. B., Paulatto, M., Kalnins, M. L., Livanos, I., and Bejelou, K.: The emergence and growth of a submarine volcano: The Kameni islands, Santorini (Greece), Geo. Res. J., 1, 8–18, 2014.

Oulas, A., Polymenakou, P. N., Seshadri, R., Tripp, H. J., Mandalakis, M., Paez-Espino, A. D., Pati, A., Chain, P., Nomikou, P., Carey, S., Kilias, S., Christakis, C., Kotoulas, G., Magoulas, A., Ivanova, N. N., and Kyrpides, N. C.: Metagenomic investigation of the geologically unique Hellenic Volcanic Arc reveals a distinctive ecosystem with unexpected physiology, Environ. Microbiol., 18, 1122–1136, 2016.

Ozawa, A., Ueda, A., Fantong, W. Y., Anazawa, K., Yoshida, Y., Kusakabe, M., Ohba, T., Tanyileke, G., and Hell, J. V.: Rate of siderite precipitation in Lake Nyos, Cameroon, Geol. Soc. London Sp. Pub., 437, 22 June 2016, https://doi.org/10.1144/SP437.13, 2016.

Papanikolaou, D., Lekkas, E., and Syskakis, D.: Tectonic analysis of the geothermal field of Milos Island, Bull. Geol. Soc. Greece, 24, 27–46, 1990.

Papavassiliou, K., Voudouris, P., Kanellopoulos, C., Glasby, G., Alfieris, D., and Mitsis, I.: New geochemical and mineralogical constraints on the genesis of the Vani hydrothermal manganese deposit at NW Milos island, Greece: Comparison with the Aspro Gialoudi deposit and implications for the formation of the Milos manganese mineralization, Ore Geol., 80, 594–611, 2017.

Paulmier, A., Ruíz-Pino, D., and Garçon, V.: The oxygen minimum zone (OMZ) off Chile as intense source of CO_2 and N_2O, Cont. Shelf. Res., 28, 2746–2756, 2008.

Paulmier, A., Ruiz-Pino, D., and Garçon, V.: CO_2 maximum in the oxygen minimum zone (OMZ), Biogeosciences, 8, 239–252, https://doi.org/10.5194/bg-8-239-2011, 2011.

Percoits, E., Gingras, M. K., Barley, M. E., Kapper, A., Posth, N. R., and Konhauser, K. O.: Petrography and geochemistry of the Dales Gorge banded iron formation: Paragenetic sequence, source and implications for palaeo-ocean chemistry, Pre. Res., 172, 163–187, 2009.

Pichler, T. and Dix, G. R.: Hydrothermal venting within a coral reef ecosystem, Ambitle Island, Papua New Guinea, Geology, 50, 435–438, 1996.

Pichler, T. and Veizer, J.: Precipitation of Fe(III) oxyhydroxide deposits from shallow-water hydrothermal fluids in Tutum Bay, Ambitle Island, Papua New Guinea, Chem. Geol., 162, 15–31, 1999.

Pichler, T. and Veizer, J.: The precipitation of aragonite from shallow-water hydrothermal fluids in a coral reef, Tutum Bay, Ambitle Island, Papua New Guinea, Chem. Geol., 207, 317–45, 2004.

Planavsky, N., Rouxel, O., Bekker, A., Shapiro, R., Fralick, P., and Knudsen, A.: Iron-oxidizing microbial ecosystems thrived in late Paleoproterozoic redox-stratified oceans, Earth Planet. Sc. Lett., 286, 2307–242, 2009.

Planavsky, N. J., Bekker, A., Rouxel, O. J., Kamber, B., Hofmann, A., Knudsen, A., and Lyons, T. W.: Rare earth element and yttrium compositions of Archean and Paleoproterozoic Fe formations revisited: New perspectives on the significance and mechanisms of deposition, Geochim. Cosmochim. Ac., 74, 6387–6405, 2010.

Plimer, I.: Milos Geologic History, Koan Publishing House, Athens, Greece, 261 pp., 2000.

Poulton, S. W. and Canfield, D. E.: Development of a sequential iron extraction procedure for iron: implications for iron partitioning in continentally derived particles, Chem. Geol., 2014, 209–221, 2005.

Poulton, S. W. and Canfield, D. E.: Ferruginous conditions: A dominant feature of the ocean through Earth's history, Elements, 7, 107–112, 2011.

Preuß, A., Schauder, R., Fuchs, G., and Stichler W.: Carbon isotope fractionation by autototrophic bacteria with three different CO_2 fixation pathways, Zeitschrift für Naturforschung C., 44, 397–402, 1989.

Rancourt, D. G., Fortin, D., Pichler, T., and Lamarche, G.: Mineralogical characterization of a natural very As-rich hydrous ferric oxide coprecipitate formed by mixing of hydrothermal fluid and sea water, Am. Min., 86, 834–851, 2001.

Rasmussen, B., Meier, D. B., Krapež, B., and Muhling, J. R.: Iron silicate microgranules as precursor sediments to 2.5-billion-year-old banded iron formations, Geology, 41, 435–438, 2013.

Rasmussen, B., Krapež, B., and Meier, D. B. Replacement origin for hematite in 2.5 Ga banded iron formation: Evidence for post-depositional oxidation of iron-bearing minerals, Geol. Soc. Am. Bull., 126, 438–446, 2014.

Riedel, T., Zak, D., Biester, H., and Dittmar, T.: Iron traps terrestrially derived dissolved organic matter at redox interfaces, P. Nat. Acad. Sci. USA, 110, 10101–10105, 2013.

Robbins, E. I., Kourtidou-Papadeli, C., Iberall, A. S., Nord Jr., G. L., and Sato, M.: From Precambrian Iron-Formation to Terraforming Mars: The JIMES Expedition to Santorini, Geomicrobiol. J., 33, 630–645, 2016.

Roy, S.: Manganese Mineralization: Geochemistry and mineralogy of terrestrial and marine deposits, Geol. Soc. Special Publucation, 119, 5–27, 1997.

Roy, S.: Sedimentary manganese metallogenesis in response to the evolution of the Earth system, Earth-Sci. Rev., 77, 273–305, 2006.

Rudnick, R. and Gao, S.: Composition of the continental crust, in: Treatise on Geochemistry, Elsevier–Pergamon, Oxford, 3, 1–64, 2003.

Schwertmann, U. and Murad, E.: Effect of pH on the formation of goethite and hematite from ferrihydrite, Clay. Clay Min., 31, 277–284, 1983.

Shanmugam, G.: Submarine fans: a critical retrospective (1950–2015), J. Palaeogeogr., 5, 110–184, 2016.

Shuster, D. L., Farley, K. A., Vasconcelos, P. M., Balco, G., Monteiro, H. S., Waltenberg, K., and Stone, J. O.: Cosmogenic 3 He in hematite and goethite from Brazilian "canga" duricrust demonstrates the extreme stability of these surfaces, Earth Planet. Sc. Lett., 329, 41–50, 2012.

Sigurdsson, H., Carey, S., Alexandri, M., Vougioukalakis, G., Croff, K., Roman, C., Sakellariou, D., Anagnostou, C., Rousakis, G., Loakim, C., Goguo, A., Ballas, D., Misaridis, T., and Nomikou, P.: Marine investigations of Greece's Santorini volcanic field, EOS T. Am. Geophy. Un., 87, 337–342, 2006.

Simonson, B. M.: Sedimentological constraints on the origins of Precambrian iron-formations, Geol. Soc. Am. Bull., 96, 244–252, 1985.

Simonson, B. M. and Hassler, S. W.: Was the deposition of large Precambrian iron formations linked to major marine transgressions?, J. Geol., 104, 665–676, 1996.

Skarpelis, N. and Koutles, T.: Geology of epithermal mineralization of the NW part of Milos Island, Greece, in:Proceedings of the 5th International Symposium on Eastern Mediterranean Geology, edited by: Chatzipetros, A. and Pavlides S., School of Geology, Aristotelian University of Thessaloniki, Thessaloniki, Greece, 1449–1452, 2004.

Smith, A. J. B., Beukes, N. J., and Gutzmer, J.: The Composition and depositional environments of Mesoarchean Iron Formations of the West Rand Group of the Witwatersrand Supergroup, South Africa, Econ. Geol., 108, 111–134, 2013.

Sperling, E. A., Wolock, C. J., Gill, B. C., Kunzmann, M., Halverson, G. P., Macdonald, F. A., Knoll, A. H., and Johnston D. T.: Statistical Analysis of Iron Geochemical Data Suggests Limited Late Proterozoic Oxygenation, Nature, 523, 451–454, 2015.

Stewart, A. L. and Mcphie, J.: Facies architecture and Late Ploicene – Pleistocene evolution of a felsic volcanic island, Milo, Greece, Bull. Volcanol., 68, 703–726, 2006.

Stüben, D. and Glasby, G. P.: Geochemistry of shallow submarine hydrothermal fluids from Paleohori Bay, Milos, Aegean Sea, Exp. Min. Geol., 8, 273–287, 1999.

Sun, S., Konhauser, K. O., Kappler, A., and Li, Y.-L.: Primary hematite in Neoarchean to Paleoproterozoic oceans, GSA Bull., 127, 850–861, 2015.

Swamy, V., Saxena, S. K., Sundman, B., and Zhang, J.: A thermodynamic assessment of silica phase diagram, J. Geophys. Res.-Sol. Ea., 99, 11787–11794, 1994.

Taylor, J. and Parkes, R. J.: The cellular fatty-acids of the sulfate-reducing bacteria, Desulfobacter sp., Desulfobulbus sp. and Desulfovibrio desulfuricans, J. Gen. Microbiol., 129, 3303–3309, 1983.

Tice, M. M. and Lowe, D. R.: The origin of carbonaceous matter in pre-3.0 Ga greenstone terrains: A review and new evidence from the 3.42 Ga Buck Reef Chert, Earth Sci. Rev., 76, 259–300, 2006.

Tiodjio, R. M., Sakatoku, A., Nakamura, A., Tanaka, A., Fantong, W. Y., Tchakam, K. B., Tanyileke, G., Ohba, T., Hell, V. J., Kusakabe, M., Nakamura, S., and Ueda, A.: Bacterial and archaeal communities in Lake Nyos (Cameroon, Central Africa), Sci. Rep.-UK, 4, 6151, https://doi.org/10.1038/srep06151, 2014.

Trendall, A. F.: The significance of iron-formation in the Precambrian stratigraphic record, Int. Assoc. Sed. Spe. Pub., 33, 33–66, 2002.

Tsikos, H., Mathews, A., Erel, Y., and Moore, J. M.: Iron isotopes constrain biogeochemical redox cycling of iron and manganese in a Palaeoproterozoic stratified basin, Earth Planet. Sc. Lett., 298, 125–134, 2010.

van Hinsbergen, D. J. J., Snel, E., Garstman, S. A., Mărunţeanu, M., Langereis, C. G., Wortel, M. J. R., and Meulenkamp, J. E.: Vertical motions in the Aegean volcanic arc: evidence for rapid subsidence preceding volcanic activity on Milos and Aegina, Mar. Geol., 209, 329–345, 2004.

Varnavas, S. P. and Cronan, D. S.: Submarine hydrothermal activity off Santorini and Milos in the Central Hellenic Volcanic Arc: A synthesis, Chem. Geol., 224, 40–54, 2005.

Weber, K. A., Achenbach, L. A., and Coates, J. D.: Microorganisms pumping iron: anaerobic microbial iron oxidation and reduction, Nat. Rev. Microbiol., 4, 752–64, 2006.